

1652  
8128

# NATIONAL ADVISORY COMMITTEE FOR AERONAUTICS

TECHNICAL NOTE

No. 1652

INVESTIGATION OF AXIAL-FLOW FAN AND COMPRESSOR  
ROTORS DESIGNED FOR THREE-DIMENSIONAL FLOW

By A. Kahane

Langley Memorial Aeronautical Laboratory  
Langley Field, Va.



Washington

July 1948

AFMDC  
TECHNICAL LIBRARY  
AFL 2811

0144987



TECH LIBRARY KAFB, NM



## TECHNICAL NOTE NO. 1652

## INVESTIGATION OF AXIAL-FLOW FAN AND COMPRESSOR

## ROTORS DESIGNED FOR THREE-DIMENSIONAL FLOW

By A. Kahane

## SUMMARY

An investigation has been conducted to determine whether three-dimensional flows may be efficiently utilized in axial-flow fan and compressor rotors so that the spanwise load distribution may be suitably varied to obtain high pressure rise. Two rotors, one with approximately uniform and one with solid-body downstream tangential-velocity distributions, were designed and tested at the design blade angle. Radial surveys of total pressure, static pressure, and flow angle were made upstream and downstream of the test rotors through a quantity-coefficient range. Tests of the solid-body rotor were also conducted at a large value of tip clearance.

The results indicated that the three-dimensional flows may be utilized with high efficiency and that the three-dimensional theory used in conjunction with two-dimensional cascade data is sufficiently accurate for design purposes. The tests also showed that the tip-clearance losses of rotors highly loaded at the tips are not excessive. The existing three-dimensional theory in simplified form and an illustrative rotor design are presented in appendixes.

## INTRODUCTION

The conventional method of blade design for axial-flow fans and compressors specifies a free-vortex type of blade loading, which is characterized by a flow through the rotor disk that is essentially two-dimensional. Tests of a series of free-vortex-designed fans are reported in reference 1; the experimental results therein show excellent agreement with the theory. For designs in which a high-pressure-rise rotor is required, use of spanwise load distributions differing from the free-vortex type may be desirable. Compressibility effects may be appreciable, however, in the determination of the most suitable load distribution of high-pressure-rise rotors.

When the blade loading is different from the free-vortex type, a three-dimensional flow may occur at the fan; this flow results in a change of axial-velocity distribution from upstream to downstream of the

blading. In order to design the rotor accurately, the axial velocity at the blades must be known. The effect of the blade load distribution on the axial-velocity profile at a rotor and stator was initially determined in reference 2 by the solution of the Euler equations. Tests of low-solidity fans are also reported in reference 2. No attempt was made to load these fans highly at the tips and, inasmuch as only total-pressure surveys were made, only limited conclusions as to the applicability of the theory to design could be drawn. An alternate method for the determination of the actual velocity distribution at a rotor in three-dimensional flow in terms of the flow angles was presented in British reports of limited circulation but the labor involved in the solution is excessive.

Two rotors with higher loading at the tips than free-vortex-type blading have been designed and tested in the Langley propeller-research-tunnel laboratory to determine whether the three-dimensional theory may be effectively used to design higher-pressure-rise rotors. The rotors were designed for upstream velocities which were both axial and uniform and for approximately constant and "solid-body" downstream absolute tangential-velocity distributions. (Solid-body notation indicates a variation of tangential velocity directly proportional to the radius.) Tests of each rotor were made at the design blade angle through a range of quantity coefficient. Radial surveys of total pressure, static pressure, and flow angle were made upstream and downstream of each test rotor. Tests of the solid-body rotor were also conducted at a large value of tip clearance to determine whether the high pressure rise at the tip would adversely affect the tip losses.

The experimental results of the present investigation are given herein and are compared with theoretically predicted values. The three-dimensional theory in a simplified form is presented in appendix A, and a rotor design procedure is illustrated in a sample calculation in appendix B.

#### SYMBOLS AND COEFFICIENTS

$c$	blade chord, feet
$B$	number of blades
$C_H$	total-pressure-rise coefficient $\left( \frac{\Delta \bar{H}}{\rho n^2 D^2} \right)$
$c_l$	section lift coefficient based on mean relative velocity
$C_p$	static-pressure-rise coefficient $\left( \frac{\Delta p}{\rho n^2 D^2} \right)$

$C_T$  torque coefficient  $\left( \frac{T}{\rho n^2 D^5} \right)$

$D$  inside diameter of fan casing, feet

$H$  total pressure, pounds per square foot

$\Delta H$  total-pressure rise, pounds per square foot

$\overline{\Delta H}$  weighted average total-pressure rise (incompressible flow assumed), pounds per square foot

$$\left( \frac{2\pi}{Q} \int_{r_h}^R r (H_2 V_{a2} - H_1 V_{a1}) dr \right)$$

$n$  rotational speed, revolutions per second

$p$  static pressure, pounds per square foot

$\Delta p$  static-pressure rise, pounds per square foot

$\overline{\Delta p}$  weighted average static-pressure rise (incompressible flow assumed), pounds per square foot

$$\left( \frac{2\pi}{Q} \int_{r_h}^R r (p_2 V_{a2} - p_1 V_{a1}) dr \right)$$

$q_a$  effective axial dynamic pressure at fan, pounds per square foot

$Q$  quantity rate of flow, cubic feet per second

$Q/nD^3$  quantity coefficient

$r$  radius, feet

$R$  radius to fan casing, feet

$T$  torque, pound-feet

$$\left( 2\pi \int_{r_h}^R \rho_2 u_2 V_{a2} r^2 dr \right)$$

$u$	absolute tangential velocity, feet per second
$V$	absolute velocity, feet per second
$V_a$	effective axial velocity at fan, feet per second
$x$	radius ratio ( $r/R$ )
$\alpha$	angle between effective relative entering air and chord line of blade, degrees
$\beta$	stagger angle; angle between the effective relative entering air and fan axis, degrees
$\delta$	tangential-velocity parameter ( $u/\omega R$ )
$\eta$	efficiency
$\eta_H$	total-pressure-rise efficiency $\left( \frac{1}{2\pi} \frac{C_H}{C_T} \frac{Q}{nD^3} \right)$
$\eta_p$	static-pressure-rise efficiency $\left( \frac{1}{2\pi} \frac{C_P}{C_T} \frac{Q}{nD^3} \right)$
$\theta$	effective turning angle, degrees
$\rho$	mass density of air, slugs per cubic foot
$\sigma$	solidity ( $Bc/2\pi r$ )
$\varphi$	flow parameter ( $V_a/\omega R$ )
$\Delta\varphi$	increment of flow parameter along radius ( $\Delta V_a/\omega R$ )
$\omega$	rotor angular velocity, radians per second

## Subscripts:

$a$	axial
$A$	a particular radius
$B$	a particular radius
$h$	hub
$o$	atmospheric

- 1           upstream of fan
- 2           downstream of fan

Bar over symbol indicates an average value.

## THEORETICAL CONSIDERATIONS

### Flow through a Rotor

In the conventional method of design of axial-flow fan and compressor blading, the blades are loaded radially so that no mutual interference exists between adjacent blade elements. This loading is accomplished by having the absolute tangential velocities in front of and behind the fan vary inversely with the radius, or

$$u = \frac{\text{Constant}}{r}$$

Because of the analogy between this tangential-velocity field and the radial variation of velocity due to a line vortex situated on the fan axis, rotors designed in such a manner are known as free-vortex rotors. The flow through free-vortex blading in incompressible flow is essentially two-dimensional in character; no radial velocities occur in the flow field outside the boundary-layer regions. In incompressible flow, therefore, the axial velocities at a particular radius are the same upstream and downstream of the fan when the flow area is constant. A free-vortex rotor is also characterized by a uniform total-energy rise across the annulus.

When the blades are loaded in a manner different from the free-vortex manner, radial velocities may be induced in the flow through them, and, if so, this flow is therefore of a three-dimensional nature. It should be pointed out that it is possible in some cases to obtain a two-dimensional-type flow with non-free-vortex loaded blading. Consider a rotor loaded so that the direction of the radial velocities is outward. The flow streamlines are therefore deflected outward. (See fig. 1.) The flow reaches a radial equilibrium behind the fan when the pressure forces balance the centrifugal forces of the rotating flow. The axial velocities have increased at the outer radii and decreased at the inner radii. Reference 2 shows that, upon assumption of an infinite number of blades, an infinitesimally thin rotor disk, and a system of trailing vortices that extend downstream to infinity in concentric cylinders, the effective axial velocity at the blade  $V_a$  is the mean of the axial

velocities at points upstream and downstream where equilibrium exists. This relation is expressed in the following equation:

$$V_a = \frac{V_{a1} + V_{a2}}{2} \quad (1)$$

The determination of the axial-velocity distribution at the blades, as given in reference 2, is presented in a simplified form for a rotor and stator in appendix A. The theory has been presented for an incompressible fluid, but the result is identical for a compressible fluid. The application of the theory is illustrated in a sample three-dimensional rotor design in appendix B.

A higher pressure rise may be obtained by loading the rotor higher at the tips than the corresponding free-vortex loaded rotor. The increase of total-pressure rise theoretically obtainable by loading a rotor, the upstream flow of which is uniform and axial, so that the tangential-velocity distribution downstream is either of the uniform or solid-body type is shown in figure 2, wherein the more heavily loaded rotors are compared with a free-vortex loaded rotor that has the same value of tangential velocity at the hub. The solid-line curves are plots of the approximate formulas derived in appendix C. The dashed curve was computed exactly for a solid-body rotor operating at  $\frac{\omega R}{V_{a1}} = 1.75$ , with

$$\left(\frac{u_2}{V_{a1}}\right)_h = 0.60, \text{ by weighting the total-pressure rise with the velocity}$$

distribution determined from equation (7). Results obtained with exact and approximate methods were in good agreement. Figure 2 indicates that extremely large increases of pressure rise may be obtained with a solid-body rotor at the lower hub-tip radius ratios.

#### Application of Cascade Data to Three-Dimensional-Flow

##### Blading Design

Because of the two-dimensional nature of the flow through a free-vortex fan, the flow through the rotating blades at a given radius is analogous to the two-dimensional flow through the corresponding cascade of airfoils (reference 3). The static-pressure rise and the total-pressure rise realized in an incompressible frictionless fluid may be written as functions of the stagger angle  $\beta$  and the turning angle  $\theta$ ; they are (see fig. 3(a)):

$$\frac{\Delta p}{q_a} = \tan^2 \beta - \tan^2(\beta - \theta)$$

$$\frac{\Delta H}{q_a} = \frac{\Delta p}{q_a} + \left(\frac{u_2}{V_a}\right)^2 - \left(\frac{u_1}{V_a}\right)^2 = \tan^2 \beta - \tan^2(\beta - \theta) + \left(\frac{u_2}{V_a}\right)^2 - \left(\frac{u_1}{V_a}\right)^2$$

When the axial velocity varies through the blades, as in three-dimensional flow, the flow is no longer similar to that through a two-dimensional cascade. The actual flow could most closely be approximated in a cascade tunnel, in which the test-section flow area was varied by diverging or converging side walls. Cascade data of this nature, however, are not available at the present time. In the absence of complete experimental information use of two-dimensional cascade data should be possible with the qualification that the stagger and turning angles are to be computed relative to the mean axial velocity, as shown in figure 3(b). The equations for the static-pressure rise and the total-pressure rise are, accordingly,

$$\frac{\Delta p}{q_a} = \tan^2 \beta - \tan^2(\beta - \theta) + \left(\frac{V_{a1}}{V_a}\right)^2 - \left(\frac{V_{a2}}{V_a}\right)^2 \quad (2)$$

$$\begin{aligned} \frac{\Delta H}{q_a} &= \frac{\Delta p}{q_a} + \left(\frac{u_2}{V_a}\right)^2 - \left(\frac{u_1}{V_a}\right)^2 - \left(\frac{V_{a1}}{V_a}\right)^2 + \left(\frac{V_{a2}}{V_a}\right)^2 \\ &= \tan^2 \beta - \tan^2(\beta - \theta) + \left(\frac{u_2}{V_a}\right)^2 - \left(\frac{u_1}{V_a}\right)^2 \end{aligned} \quad (3)$$

## APPARATUS

### Test Setup

The general arrangement of the test setup, a modification of the equipment of reference 4, is shown in figures 4 and 5. The fan blades were mounted in the 24-blade hub used in the tests of reference 4. The power for the fan was supplied by a 25-horsepower, water-cooled, alternating-current electric motor. The fan casing at the test section was of rolled and welded steel plate bored to a diameter of 21 inches. The radial-survey instruments were mounted in this casing 4 inches ahead of and behind the rotor center line and were spaced about 120° apart. The rear survey instrument was located about 1.4 chord lengths behind the blade trailing



edges. The instruments (fig. 6) consisted of a total-pressure tube, a static-pressure tube, and a yaw head mounted in a single  $\frac{1}{4}$ -inch tube that could be moved along and rotated about a radial axis. A scale and calibrated knob permitted the reading of the radial position of the tube to 0.001 inch, and the angular position of the tube could be read on a protractor and vernier to  $0.1^\circ$ .

Preliminary tests with the bell inlet of reference 4 indicated that severe fluctuations of flow existed and that these fluctuations prevented accurate angular readings with the yaw heads. An inlet with a 10:1 area contraction and three screens was then installed and found satisfactory.

The diffuser and throttle downstream were the same as those used in the tests of reference 4.

### Test Fans

The rotors investigated are designated fans 1, 2, and 2a. The tip clearance of fans 1 and 2 was about 0.015 inch. The tip clearance of fan 2a was about 0.063 inch; in other respects fan 2a was identical with fan 2. Each fan consisted of 24 blades of constant chord equal to 2.32 inches and of nominal span equal to  $3\frac{1}{4}$  inches. The ratio of the hub and tip radii was 0.69. The solidity at the pitch section (located halfway between the inner and outer walls) was 1.0. The blade sections were of the 10-percent-thick NACA 65-series blower-blade sections investigated in cascade in references 3 and 5. Drawings of the blades are shown in figure 7 and the section ordinates are given in table I.

Fan 1 was designed for a constant section lift coefficient  $c_l$  of 0.7 along the blade at a value of the design quantity coefficient  $Q/nD^3$  of 0.587. This  $c_l$  distribution corresponded to an approximately constant absolute tangential-velocity distribution downstream of the blades at the design point. A second fan with the same solidity as that of fan 1 was designed for a solid-body tangential-velocity distribution at a value of  $Q/nD^3$  of 0.587. Preliminary calculations indicated that a slightly twisted blade with uniform section along the span would give the desired result. For simplicity of construction, therefore, fan 2 was built as a straight blade with the NACA 65-(12)10 blower-blade section along the span. The blade characteristics and theoretical performance characteristics of fans 1 and 2 are presented in figure 8.

### TEST METHOD

Before the actual fan tests were made, the static-pressure tube was calibrated to determine the interference effects. The yaw-head zeros were

determined by removing the test fan, sealing the gap, and drawing air through the setup with a blower.

The tests were conducted at a fan rotational speed of about 3000 rpm. The quantity flow was regulated with the exit throttle. At each of from 18 to 20 stations along the radius, the front and rear survey tubes were rotated until "null" readings were obtained on the U-tube manometers connected to the yaw heads. Readings of total pressure, static pressure, survey-tube radial position and angle, wet- and dry-bulb temperatures, and rotational speed were then taken. The barometer was read before and after a run. Inasmuch as the speed of the drive motor tended to vary during a test, readings were taken only when the rotational speed was within  $\pm 10$  rpm of that specified for the test.

The power input was measured by the amount of rotation put into the air. The quantity flow, the total-pressure rise, and the static-pressure rise were determined by integration of the survey measurements.

The tests were conducted at a Reynolds number (based on blade chord) of approximately 350,000 and a Mach number of about 0.24. These values of Reynolds number and Mach number were both based on mean relative velocity.

## RESULTS AND DISCUSSION

### Over-All Fan Characteristics

The fan-characteristic curves of the three configurations investigated are presented in figure 9. Comparison of the experimental coefficients at the design point  $\left(\frac{Q}{nD^3} = 0.587\right)$  with the theoretically predicted coefficients of fans 1 and 2 are shown in the following table:

Coefficient	Fan 1		Fan 2	
	Theory	Experiment	Theory	Experiment
$C_H$	2.43	2.63	3.58	3.51
$C_P$	1.99	1.97	2.56	2.48
$C_T$	.240	.258	.352	.348
$\eta_H$	-----	.935	-----	.942
$\eta_P$	-----	.718	-----	.666

The agreement between experiment and theory is considered good. The high values of total-pressure efficiency obtained indicated that no large mixing loss is associated with the three-dimensional flow.

The effect of the increased tip clearance of fan 2a was to decrease the value of  $\eta_H$  at the design point about 3 percent. Fans loaded highly at the tips do not appear to be subject to excessive tip-clearance losses.

The surge points of fans 2 and 2a, as indicated by the smallest quantity coefficient at which data could be taken, occurred at values of  $Q/nD^3$  of about 0.50 and 0.52, respectively. These values indicate that the effect of the increased tip clearance was to reduce the operating range of the fan.

### Surveys

Fans 1 and 2.— The results of the surveys of fans 1 and 2 are presented in figures 10 and 11, respectively, as plots of the radial distributions of the total and static pressures in front of and behind the fans, the tangential and axial velocities downstream of the blades, and the stagger and turning angles, each at several values of the quantity coefficient  $Q/nD^3$ .

The distribution of total pressure upstream of the fans (figs. 10(a) and 11(a)) was essentially uniform outside the boundary-layer region. The total-pressure distributions downstream of the blades are characterized by low-energy regions at the walls, which are the result of losses due to secondary flows, tip clearance, and the rotating hub. These distributions also indicate that the blade loading is shifted toward the tips as the quantity flow is decreased.

The static-pressure distributions upstream of the fans (figs. 10(b) and 11(b)) were essentially uniform. The sudden rise of static-pressure coefficient near the boundaries appears to be the result of wall interference on the static-pressure-tube reading. The static-pressure gradient downstream of the rotor increases with decreasing quantity coefficient. This increase is as expected, since the static-pressure gradient when radial equilibrium is attained (see equation (6)) is

$$\frac{dp_2}{dr} = \rho_2 \frac{u_2^2}{r}$$

and  $u_2$  varies directly with the loading.

The survey measurements indicated that the tangential velocities upstream of the rotor were essentially zero. The tangential velocities downstream of fans 1 and 2 are presented in figures 10(c) and 11(c). The tangential velocities downstream of fan 1 decrease generally with distance from the inner wall, whereas the tangential velocities downstream of fan 2 show a general increase with distance from the inner wall.

The upstream total-pressure and static-pressure distributions of figures 10(a), 10(b), 11(a), and 11(b) indicate that the axial-velocity distribution ahead of the rotor was essentially uniform. Distributions of axial velocity downstream of fans 1 and 2 are presented in figures 10(d) and 11(d). The profiles are all characterized by low-velocity regions at the walls. At a value of  $Q/nD^3$  of 0.710 the axial velocities downstream of fan 1 are essentially uniform. At values of  $Q/nD^3$  less than 0.710 the axial velocities outside the boundary regions increase with distance from the inner wall, whereas the reverse is true for values of  $Q/nD^3$  greater than 0.710. The axial velocities downstream of fan 2 increase with distance from the inner wall throughout the entire operating range. The axial-velocity gradients of fan 2 were larger than those of fan 1 inasmuch as the tips were more heavily loaded.

The stagger-angle distributions of fans 1 and 2 are presented in figures 10(e) and 11(e). The rise of stagger angle near the walls is associated with the axial-velocity defect in the boundary regions. In general, because of the steeper axial-velocity gradients of fan 2, the stagger-angle distributions of this fan are flatter than those of fan 1.

The turning-angle distributions of fans 1 and 2 are shown in figures 10(f) and 11(f). These distributions are characterized by a sharp increase and then a decrease of turning angle near the inner wall and a decrease near the outer wall. The rise of turning angle near the inner wall is probably the result of an increase of angle of attack on the blade section, which is caused by the low effective axial velocity in that region. The decrease of turning angle immediately adjacent to both walls occurs probably because of the predominating effect of the losses close to the wall. The turning angles of both fans decrease in general with distance from the inner wall, but the gradient is slight for fan 2.

Comparison of design-point experimental surveys with theory.- A comparison of the experimental survey results at the design point with the theoretically predicted values is shown in figures 12(a) and 12(b) for fans 1 and 2, respectively. The downstream axial-velocity and total-pressure-rise gradients obtained experimentally with fan 1 differ slightly from those predicted because of the deviation of the experimental and theoretical tangential-velocity distributions. The downstream axial-velocity, total-pressure-rise, and tangential-velocity gradients obtained with fan 2 show good agreement with the theoretical slopes outside the boundary regions. For the hub-tip radius ratio of these tests ( $x_h = 0.69$ ) the boundary-loss effects upon the total-pressure-rise and axial-velocity

distributions appear to be secondary to the effect of load distribution. The agreement between the theoretical and experimental values is considered good and indicates that the three-dimensional theory may effectively be used for design purposes.

Calculations of the downstream static-pressure gradient at the design point of fans 1 and 2 were made by use of the equation for radial equilibrium

$$p_{2B} - p_{2A} = \int_{r_A}^{r_B} \rho_2 \frac{u_2^2}{r} dr$$

and experimentally obtained values of tangential velocity. These values are compared with the measured static-pressure distributions in figure 13, the theoretical curve having been arbitrarily placed so as to intersect the experimental points at the center of the annulus. The resulting good agreement indicates that radial equilibrium existed at the rear survey station.

Effect of increased tip clearance.— The results of the surveys of fan 2a are presented in figure 14. The distributions are similar to those of fan 2 except for slight irregularities near the outer wall. In figure 15 surveys of fans 2 and 2a are compared at a value of  $Q/nD^3$  of 0.586. The values for fan 2a in figure 15 were obtained by interpolation. The increased tip clearance decreased the total-pressure rise and downstream axial velocities near the outer wall. Inasmuch as the quantity coefficients were the same, the axial velocities downstream were larger for fan 2a than for fan 2 throughout the remainder of the annulus. This effect decreased the angle of attack, the turning angle, and therefore the total-pressure-rise coefficient in the inner region of the annulus. The comparisons show that, for the tip clearances investigated, the three-dimensional theory could be used with similar accuracy for large and small tip clearances.

## CONCLUSIONS

An investigation in the Langley propeller-research-tunnel laboratory of two axial-flow rotors, one with approximately uniform and one with solid-body downstream tangential-velocity distributions indicated that:

1. High-efficiency axial-fan and compressor blading may be designed incorporating three-dimensional flows; the use of such flows allows variation of spanwise load distribution to obtain higher pressure rise.

2. The three-dimensional theory used in conjunction with two-dimensional cascade data is sufficiently accurate for design purposes.

3. The tip-clearance losses of rotors loaded highly at the tips are not excessive.

Langley Memorial Aeronautical Laboratory  
National Advisory Committee for Aeronautics  
Langley Field, Va., March 10, 1948

## APPENDIX A

## DETERMINATION OF AXIAL-VELOCITY DISTRIBUTION

## IN THREE-DIMENSIONAL FLOW THROUGH

## A ROTOR AND STATOR

Consider the flow of an incompressible fluid through a rotor. The total-pressure rise of the flow in a stream tube may be expressed from Euler's turbine formula (reference 2) as

$$H_2 - H_1 = \eta_H \rho a r (u_2 - u_1) \quad (4)$$

In this equation the radial displacement of the stream tube is neglected. Inasmuch as

$$H_1 = p_1 + \frac{\rho}{2} v_{a1}^2 + \frac{\rho}{2} u_1^2$$

and

$$H_2 = p_2 + \frac{\rho}{2} v_{a2}^2 + \frac{\rho}{2} u_2^2$$

equation (4) can be written

$$p_2 - p_1 + \frac{\rho}{2} v_{a2}^2 - \frac{\rho}{2} v_{a1}^2 + \frac{\rho}{2} u_2^2 - \frac{\rho}{2} u_1^2 = \eta_H \rho a r (u_2 - u_1)$$

Differentiating this equation with respect to the radius results in

$$\begin{aligned} \frac{dp_2}{dr} - \frac{dp_1}{dr} + \rho v_{a2} \frac{dv_{a2}}{dr} - \rho v_{a1} \frac{dv_{a1}}{dr} + \rho u_2 \frac{du_2}{dr} - \rho u_1 \frac{du_1}{dr} \\ = \rho \omega \left[ \frac{d(\eta_H r u_2)}{dr} - \frac{d(\eta_H r u_1)}{dr} \right] \end{aligned} \quad (5)$$

If stations 1 and 2 are chosen at points where radial equilibrium of the flow exists, the pressure gradient of the rotating-air particles balances the centrifugal force due to rotation, or (see reference 2)

$$\frac{dp}{dr} = \rho \frac{u^2}{r} \quad (6)$$

Substitution of equation (6) in equation (5) results in

$$\begin{aligned} v_{a2} dv_{a2} = \omega \left[ d(\eta_H r u_2) - d(\eta_H r u_1) \right] + v_{a1} dv_{a1} + u_1 du_1 - u_2 du_2 \\ + \frac{u_1^2}{r} dr - \frac{u_2^2}{r} dr \end{aligned}$$

Integration between the limits of radii  $r_A$  and  $r_B$  gives

$$\begin{aligned} v_{a2B}^2 - v_{a2A}^2 = 2\omega \left[ (\eta_H r)_B (u_{2B} - u_{1B}) - (\eta_H r)_A (u_{2A} - u_{1A}) \right] \\ + \left( v_{a1B}^2 - v_{a1A}^2 \right) + \left( u_{1B}^2 - u_{1A}^2 \right) - \left( u_{2B}^2 - u_{2A}^2 \right) \\ + 2 \int_{r_A}^{r_B} \frac{u_1^2}{r} dr - 2 \int_{r_A}^{r_B} \frac{u_2^2}{r} dr \end{aligned} \quad (7)$$



Equation (7) indicates that, when the conditions upstream of the rotor and the downstream tangential-velocity distribution are known, the difference in axial velocities at two radial positions downstream of the fan may be determined. With the introduction of the dimensionless parameters

$$\varphi = \frac{V_a}{\omega R} \quad x = \frac{r}{R} \quad \vartheta = \frac{u}{\omega R}$$

equation (7) becomes

$$\begin{aligned} \varphi_{2B}^2 - \varphi_{2A}^2 = & 2 \left[ (\eta_H x)_B (\vartheta_{2B} - \vartheta_{1B}) - (\eta_H x)_A (\vartheta_{2A} - \vartheta_{1A}) \right] \\ & + (\varphi_{1B}^2 - \varphi_{1A}^2) + (\vartheta_{1B}^2 - \vartheta_{1A}^2) - (\vartheta_{2B}^2 - \vartheta_{2A}^2) \\ & + 2 \int_{r_A}^{r_B} \frac{\vartheta_1^2}{x} dx - 2 \int_{r_A}^{r_B} \frac{\vartheta_2^2}{x} dx \end{aligned} \quad (8)$$

When a functional relationship exists between  $\vartheta$  and  $x$ , the integrals in equation (8) may be evaluated analytically; otherwise, a graphical integration can be performed. The integrals may also be evaluated with good accuracy by considering the area under the curve a trapezoid, or

$$2 \int_{r_A}^{r_B} \frac{\vartheta^2}{x} dx = \left[ \left( \frac{\vartheta^2}{x} \right)_B + \left( \frac{\vartheta^2}{x} \right)_A \right] (x_B - x_A)$$

For most purposes it is also sufficiently accurate to assume a value of  $\eta_H = 1.00$ .

The axial-velocity distribution is obtained by first solving for the differences of the parameter  $\varphi_2$  along the radius by use of equation (8).

When a  $\Delta\varphi_2$  distribution is known, the  $\varphi_2$  variation that satisfies the equation of continuity

$$\int_{x_h^2}^{1.0} \rho_1 \varphi_1 dx^2 = \int_{x_h^2}^{1.0} \rho_2 \varphi_2 dx^2$$

can be determined. (See appendix B.) When a  $\vartheta_2$  distribution is known, the  $\varphi_2$  distribution can be obtained directly. When it is required that the axial-velocity distribution of a particular rotor be calculated, a  $\varphi_2$  distribution must be assumed and the corresponding  $\vartheta_2$  distribution calculated, until by successive approximations distributions of  $\varphi_2$  and  $\vartheta_2$  are obtained that satisfy all boundary and flow conditions. Usually only three calculations are necessary, and the labor is by no means prohibitive.

The axial-velocity-distribution equation for three-dimensional flow through a frictionless stator may be determined by setting  $\omega = 0$  in equation (7) as follows:

$$\begin{aligned} \varphi_{2B}^2 - \varphi_{2A}^2 &= (\varphi_{1B}^2 - \varphi_{1A}^2) + (\vartheta_{1B}^2 - \vartheta_{1A}^2) - (\vartheta_{2B}^2 - \vartheta_{2A}^2) \\ &+ 2 \int_{r_A}^{r_B} \frac{\vartheta_1^2}{x} dx - 2 \int_{r_A}^{r_B} \frac{\vartheta_2^2}{x} dx \end{aligned}$$

The value of  $\omega$  used in the dimensionless parameters  $\varphi$  and  $\vartheta$  in the foregoing equation may be that for the rotor used in conjunction with the stator. The actual velocity distribution is again found by satisfying the continuity relation.

## APPENDIX B

ILLUSTRATIVE DESIGN OF A THREE-  
DIMENSIONAL-FLOW ROTOR

In order to illustrate the use of the three-dimensional-flow equations of appendix A, a rotor with solid-body tangential-velocity distribution is designed. The flow is assumed to be incompressible and frictionless and the velocities upstream of the rotor are assumed to be uniform and axial. The following data are also assumed:

Hub-tip radius ratio $\left(x_h = \frac{r_h}{R}\right)$ . . . . .	0.60
Axial velocity upstream of rotor, $V_{a1}$ , feet per second . . . . .	200
Peripheral velocity of tip, $\omega R$ , feet per second . . . . .	300
Hub tangential velocity downstream of rotor, $u_{2h}$ , feet per second . . . . .	90
Solidity $\left(\sigma = \frac{Bc}{2\pi r}\right)$ . . . . .	1.0

The design computations are shown in table II.

The determination of the axial-velocity distribution is accomplished by using equation (8) of appendix A. For solid-body tangential-velocity distribution downstream of the rotor, uniform and axial entering velocities, and frictionless flow, equation (8) reduces to

$$\varphi_{2B} - \varphi_{2A} = \frac{1}{\varphi_1} \left[ (x\vartheta_2)_B - (x\vartheta_2)_A - \left( \vartheta_{2B}^2 - \vartheta_{2A}^2 \right) \right] \quad (9)$$

since

$$\varphi_{2B}^2 - \varphi_{2A}^2 = (\varphi_{2B} + \varphi_{2A})(\varphi_{2B} - \varphi_{2A})$$

$$\approx 2\varphi_1 (\varphi_{2B} - \varphi_{2A})$$

and

$$2 \int_{r_A}^{r_B} \frac{\phi_2^2}{x} dx = \phi_{2B}^2 - \phi_{2A}^2$$

The change in  $\phi_2$  is determined from equation (9) between the radial limits  $r_B$  and  $r_A$  corresponding to  $x_B = 1.00$ ,  $x_A = 0.80$ , and  $x_B = 0.80$ ,  $x_A = 0.60$ , respectively. The results are as follows:

$$x_B = 1.00 \quad x_A = 0.80$$

$$\phi_{2B} - \phi_{2A} = 0.135$$

$$x_B = 0.80 \quad x_A = 0.60$$

$$\phi_{2B} - \phi_{2A} = 0.105$$

A plot of  $\Delta\phi_2$  against  $x^2$  is then made with  $\Delta\phi_2$  assumed equal to 0 at  $x = 0.60$ ; and  $\overline{\Delta\phi_2}$  is determined by graphically evaluating the integral

$$\overline{\Delta\phi_2} = \frac{1}{1 - x_h^2} \int_{x_h^2}^{1.0} \Delta\phi_2 dx^2 \quad (10)$$

Values of  $\varphi_2$  that satisfy the continuity relation are then determined at the three radii by use of the equation

$$\varphi_2 = \varphi_1 + \Delta\varphi_2 - \overline{\Delta\varphi_2} \quad (11)$$

Values of stagger angle  $\beta$  and turning angle  $\theta$  that satisfy the required operating condition are found and the rotor performance is calculated. The blade sections were selected from the design charts of the NACA 65-series blower-blade sections (reference 3).

## APPENDIX C

INCREASE OF TOTAL-PRESSURE RISE OBTAINABLE WITH SOLID-BODY  
AND CONSTANT-TANGENTIAL-VELOCITY ROTORS

The weighted average total-pressure rise obtained with a rotor having uniform axial entering flow is, if frictionless incompressible flow is assumed,

$$\overline{\Delta H} = \frac{1}{Q} \int_0^Q \rho \omega r u_2 dQ = \frac{2\pi\rho\omega}{Q} \int_{r_h}^R r^2 u_2 V_{a2} dr \quad (12)$$

For a free-vortex loaded constant-flow-area rotor

$$u_2 = \frac{\text{Constant}}{r} = \frac{u_{2h} r_h}{r}$$

$$V_{a2} = V_{a1} = \text{Constant}$$

Substituting in equation (12) leads to

$$\begin{aligned} \overline{\Delta H}_{\text{free-vortex}} &= \frac{2\pi\rho\omega V_{a1} u_{2h} r_h}{Q} \int_{r_h}^R r dr \\ &= \frac{\pi R^3 \rho \omega V_{a1} u_{2h} x_h}{Q} (1 - x_h^2) \\ &= \rho \omega u_{2h} R x_h \end{aligned} \quad (13)$$

An expression for the total-pressure rise obtainable with a rotor loaded in the solid-body manner is determined by substituting in equation (12) the following:

$$u_2 = \text{Constant} \times r$$

$$= \frac{u_{2h}}{r_h} r$$

Thus

$$\overline{\Delta H}_{\text{solid-body}} = \frac{2\pi\rho\omega u_{2h}}{Qr_h} \int_{r_h}^R r^3 V_{a2} dr \quad (14)$$

The integral in equation (14) may be evaluated by determining the  $V_{a2}$  distribution for a particular rotor from equation (9) in appendix B. Equation (14) may be evaluated approximately by considering

$$V_{a2} = V_{a1} = \text{Constant}$$

or

$$\begin{aligned} \overline{\Delta H}_{\text{solid-body}} &\approx \frac{2\pi\rho\omega V_{a1} u_{2h}}{Qr_h} \int_{r_h}^R r^3 dr \\ &\approx \frac{\pi R^3 \rho \omega V_{a1} u_{2h}}{2Qx_h} (1 - x_h^4) \\ &\approx \frac{\rho \omega u_{2h} R (1 + x_h^2)}{2x_h} \end{aligned} \quad (15)$$

The ratio of the total-pressure rise obtainable with a solid-body rotor to the total-pressure rise obtainable with a corresponding free-vortex rotor with the same tangential velocity at the hub is approximately

$$\frac{\overline{\Delta H}_{\text{solid-body}}}{\overline{\Delta H}_{\text{free-vortex}}} \approx \frac{1 + x_h^2}{2x_h^2} \quad (16)$$

Similarly, the energy rise obtained with a constant-tangential-velocity rotor is approximately

$$\begin{aligned} \overline{\Delta H}_{u_2=\text{Constant}} &\approx \frac{2}{3} \frac{\pi R^3 \rho \omega a_1 u_{2h}}{Q} (1 - x_h^3) \\ &\approx \frac{2}{3} \rho \omega u_{2h} R \frac{1 - x_h^3}{1 - x_h^2} \end{aligned}$$

and the ratio of energy rise is

$$\frac{\overline{\Delta H}_{u_2=\text{Constant}}}{\overline{\Delta H}_{\text{free-vortex}}} \approx \frac{2(1 - x_h^3)}{3x_h(1 - x_h^2)} \quad (17)$$



## REFERENCES

1. Bogdonoff, Seymour M., and Herrig, L. Joseph: Performance of Axial-Flow Fan and Compressor Blades Designed for High Loadings. NACA TN No. 1201, 1947.
2. Ruden, P.: Investigation of Single Stage Axial Fans. NACA TM No. 1062, 1944.
3. Bogdonoff, Seymour M., and Bogdonoff, Harriet E.: Blade Design Data for Axial-Flow Fans and Compressors. NACA ACR No. 15F07a, 1945.
4. Bell, E. Barton, and DeKoster, Lucas J.: Test of a Dual-Rotation Axial-Flow Fan. NACA ARR, Dec. 1942.
5. Bogdonoff, Seymour M., and Hess, Eugene E.: Axial-Flow Fan and Compressor Blade Design Data at  $52.5^\circ$  Stagger and Further Verification of Cascade Data by Rotor Tests. NACA TN No. 1271, 1947.

TABLE I  
BLADE SECTION ORDINATES

NACA 65-(5.5)10 blower-blade section			
Upper surface		Lower surface	
Station (in.)	Ordinate (in.)	Station (in.)	Ordinate (in.)
0.008	0.020	0.016	-0.011
.013	.025	.022	-.016
.024	.032	.034	-.019
.052	.048	.064	-.024
.109	.071	.123	-.031
.167	.090	.181	-.035
.225	.105	.239	-.039
.341	.130	.355	-.044
.458	.148	.470	-.047
.575	.163	.585	-.049
.692	.174	.700	-.050
.809	.181	.815	-.050
.926	.186	.930	-.049
1.043	.187	1.045	-.047
1.160	.183	1.160	-.043
1.277	.176	1.275	-.036
1.394	.165	1.390	-.028
1.510	.150	1.506	-.018
1.627	.132	1.621	-.008
1.743	.114	1.731	0
1.859	.094	1.853	.008
1.974	.072	1.970	.014
2.090	.050	2.086	.016
2.205	.028	2.203	.012
2.321	.003	2.319	-.003
L.E. radius: 0.015		T.E. radius: 0.003	

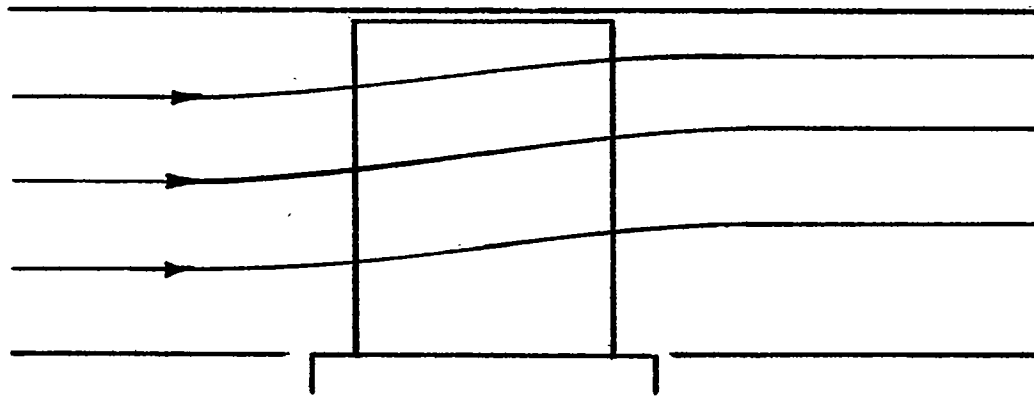
NACA 65-(7.5)10 blower-blade section			
Upper surface		Lower surface	
Station (in.)	Ordinate (in.)	Station (in.)	Ordinate (in.)
0.006	0.021	0.017	-0.012
.012	.026	.023	-.014
.022	.035	.036	-.016
.050	.052	.066	-.019
.107	.078	.125	-.023
.165	.099	.183	-.025
.223	.117	.241	-.027
.339	.145	.357	-.028
.456	.167	.472	-.028
.573	.184	.587	-.028
.690	.196	.702	-.027
.808	.205	.816	-.026
.925	.210	.931	-.024
1.043	.212	1.045	-.021
1.160	.209	1.160	-.017
1.277	.201	1.275	-.011
1.394	.189	1.390	-.003
1.511	.174	1.505	.006
1.628	.155	1.620	.014
1.744	.135	1.736	.021
1.860	.112	1.852	.027
1.975	.087	1.969	.030
2.090	.062	2.086	.028
2.205	.036	2.203	.019
2.321	.003	2.319	-.003
L.E. radius: 0.015		T.E. radius: 0.003	

NACA 65-(9.5)10 blower-blade section			
Upper surface		Lower surface	
Station (in.)	Ordinate (in.)	Station (in.)	Ordinate (in.)
0.005	0.022	0.018	-0.011
.010	.027	.025	-.012
.021	.037	.037	-.013
.048	.056	.068	-.015
.105	.085	.127	-.015
.162	.108	.186	-.015
.220	.128	.244	-.014
.337	.160	.359	-.012
.454	.185	.474	-.010
.571	.204	.589	-.007
.689	.219	.703	-.005
.807	.229	.817	-.002
.924	.235	.932	.001
1.042	.237	1.046	.004
1.160	.235	1.160	.009
1.278	.227	1.274	.015
1.395	.214	1.389	.022
1.512	.198	1.504	.029
1.629	.177	1.619	.037
1.745	.155	1.735	.042
1.860	.130	1.852	.045
1.976	.103	1.968	.045
2.091	.074	2.085	.040
2.206	.043	2.202	.027
2.321	.003	2.319	-.003
L.E. radius: 0.015		T.E. radius: 0.003	

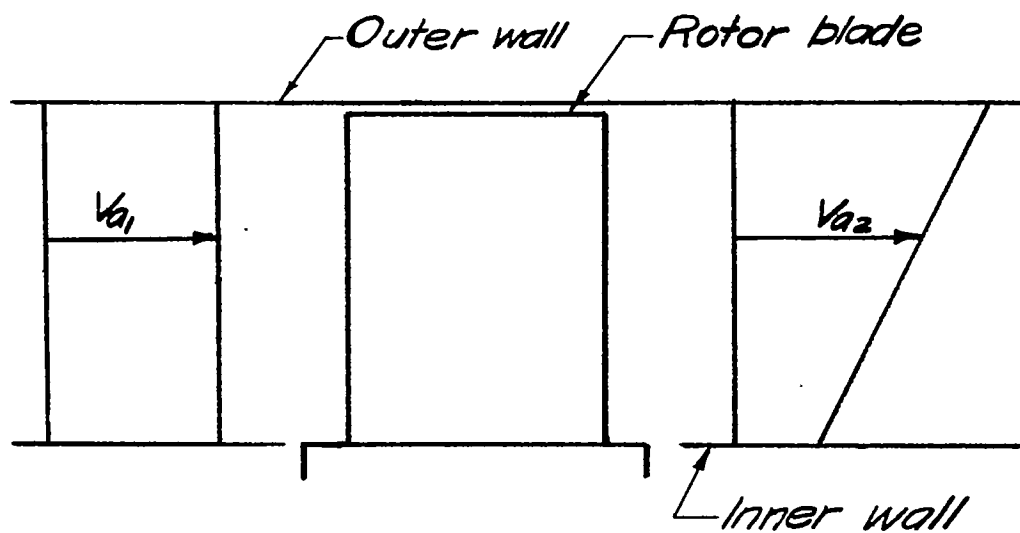
NACA 65-(12)10 blower-blade-section			
Upper surface		Lower surface	
Station (in.)	Ordinate (in.)	Station (in.)	Ordinate (in.)
0.004	0.023	0.019	-0.009
.009	.028	.026	-.009
.019	.039	.039	-.009
.046	.060	.070	-.009
.102	.094	.130	-.002
.217	.143	.247	.001
.334	.179	.362	.008
.452	.208	.477	.014
.569	.230	.591	.019
.687	.247	.705	.024
.805	.259	.819	.028
.923	.266	.933	.032
1.042	.269	1.046	.036
1.160	.267	1.160	.041
1.278	.258	1.274	.046
1.396	.245	1.388	.053
1.513	.227	1.503	.059
1.630	.206	1.618	.065
1.746	.181	1.734	.063
1.862	.153	1.850	.068
1.977	.122	1.967	.065
2.092	.089	2.084	.055
2.206	.052	2.202	.036
2.322	.003	2.318	-.003
L.E. radius: 0.015		T.E. radius: 0.003	

TABLE II  
ILLUSTRATIVE ROTOR DESIGN

Item	Source	Calculated values		
(1) $x = \frac{r}{R}$	Specified	0.60	0.80	1.00
(2) $s_2 = \frac{u_2}{\omega R}$	$s_2 = \frac{s_{2h}}{x_h} x$	.30	.40	.50
(3) $\phi_1 = \frac{v_{a1}}{\omega R}$	Specified	.667	.667	.667
(4) $\Delta\phi_2$	Equation (9)	0	.105	.240
(5) $\overline{\Delta\phi}_2$	Equation (10)	.120	.120	.120
(6) $\phi_2 = \frac{v_{a2}}{\omega R}$	Equation (11)	.547	.652	.787
(7) $\phi = \frac{v_a}{\omega R} = \frac{\phi_1 + \phi_2}{2}$	$\frac{\text{Item (3)} + \text{Item (6)}}{2}$	.607	.659	.727
(8) $\tan \beta = \frac{\pi}{\phi}$	$\frac{\text{Item (1)}}{\text{Item (7)}}$	.988	1.213	1.374
(9) $\tan (\beta - \theta)$ $= \tan \beta - \frac{s^2}{\phi}$	$\text{Item (8)} - \frac{\text{Item (2)}}{\text{Item (7)}}$	.494	.606	.686
(10) $\Delta p/q_a$	Equation (2)	1.121	1.156	1.089
(11) $\Delta H/q_a$	Equation (3)	.975	1.476	1.892
(12) $\Delta p/q_{a1}$	$\text{Item (10)} \frac{\text{Item (7)}^2}{\text{Item (3)}^2}$	.93	1.13	1.29
(13) $\Delta H/q_{a1}$	$\text{Item (11)} \frac{\text{Item (7)}^2}{\text{Item (3)}^2}$	0.81	1.44	2.25
(14) $\beta$ , deg	$\tan^{-1}$ Item (8)	44.6	50.5	54.0
(15) $\theta$ , deg	$\text{Item (14)} - \tan^{-1} \text{Item (9)}$	18.3	19.3	19.6
(16) $\sigma = \frac{Bc}{2\pi r}$	Specified	1.0	1.0	1.0
(17) Design camber of NACA 65-series blower-blade sections	Items (14), (15), (16), fig. 41(a) of reference 3	1.00	1.20	1.25
(18) $\alpha$ , deg	Items (14), (16), (17), fig. 41(b) of reference 3	13.5	14.8	15.2
(19) Blade angle, deg	Item (18) + (90 - Item (14))	58.9	54.3	51.2



(a) Flow streamlines.



(b) Axial-velocity profiles.

NATIONAL ADVISORY  
COMMITTEE FOR AERONAUTICS

Figure 1.- Flow streamlines and axial-velocity profiles in three-dimensional frictionless flow through a rotor.

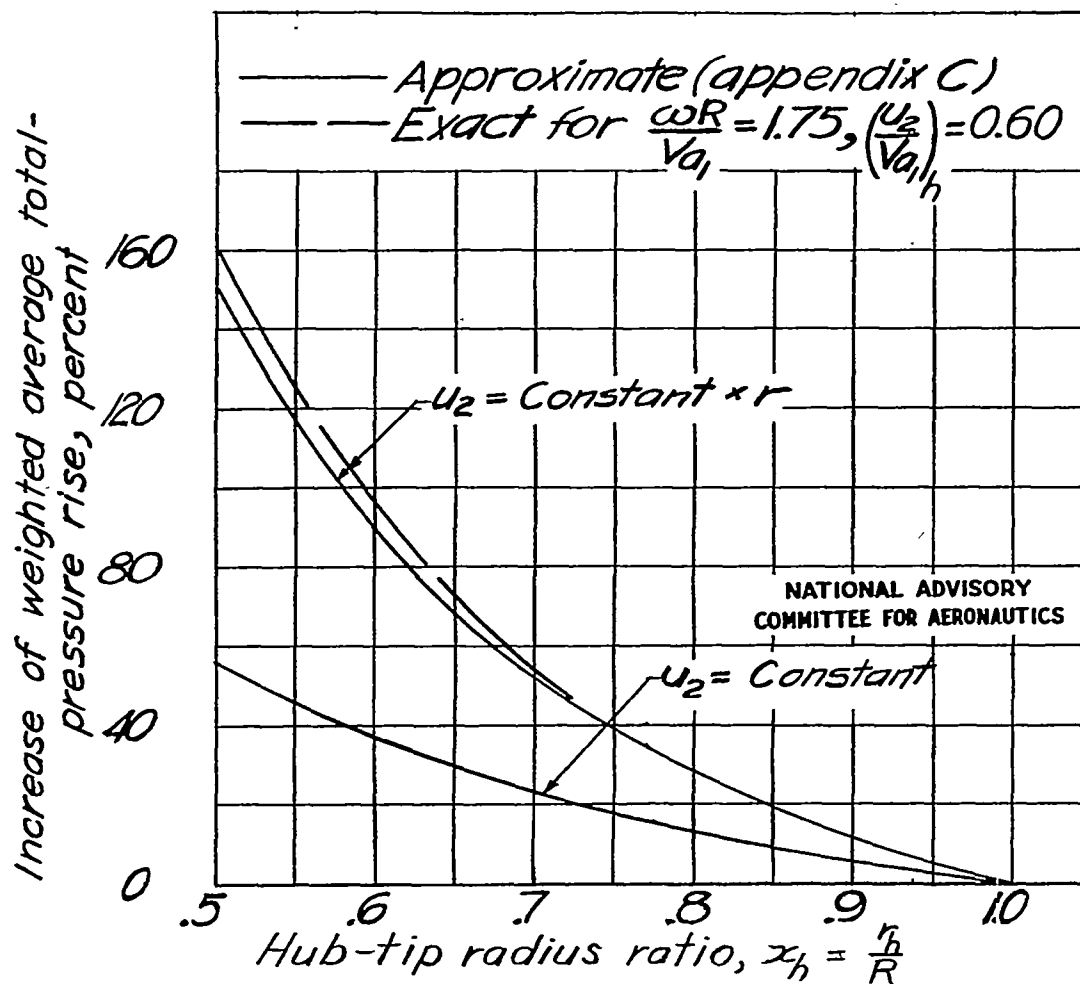
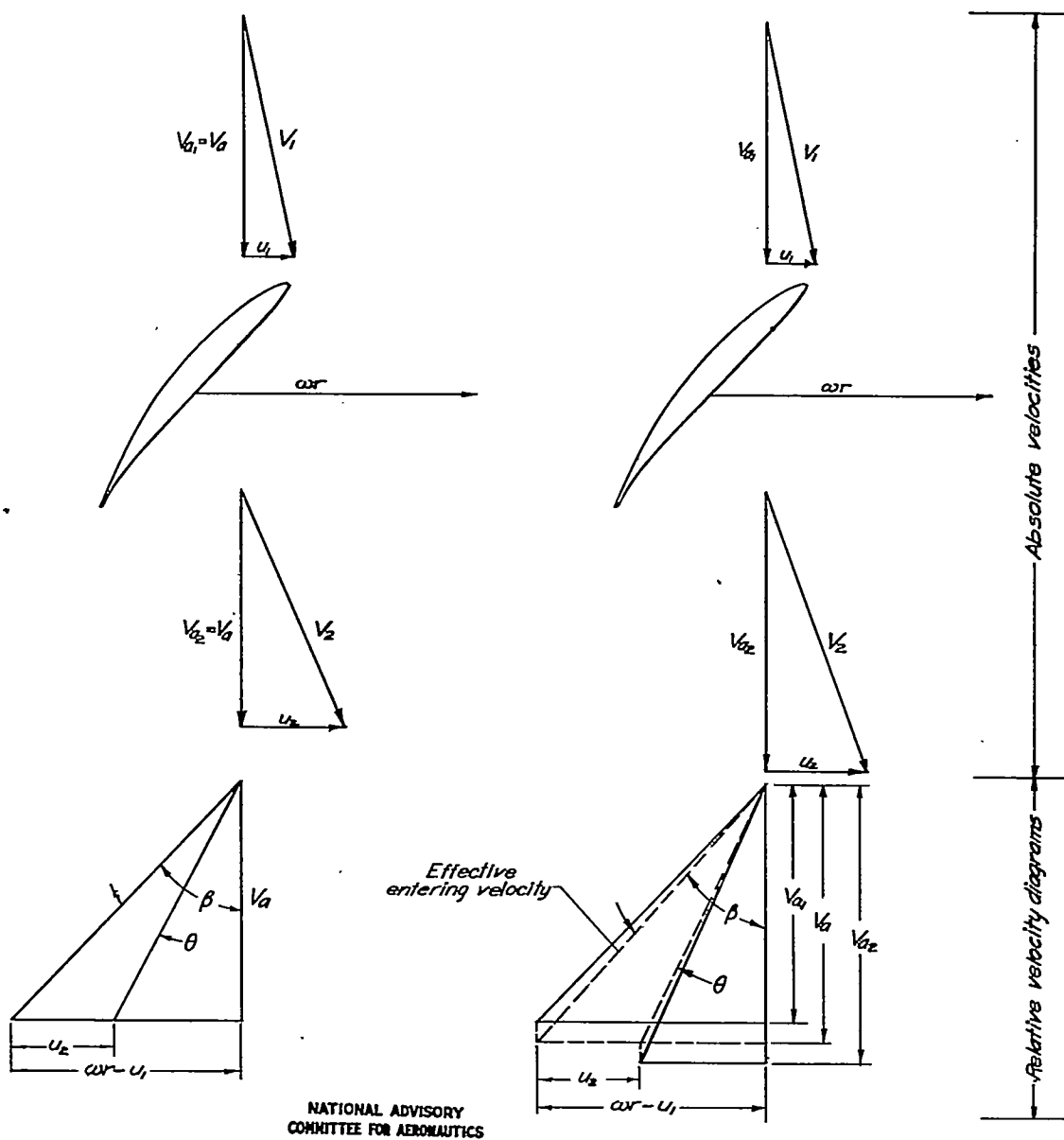


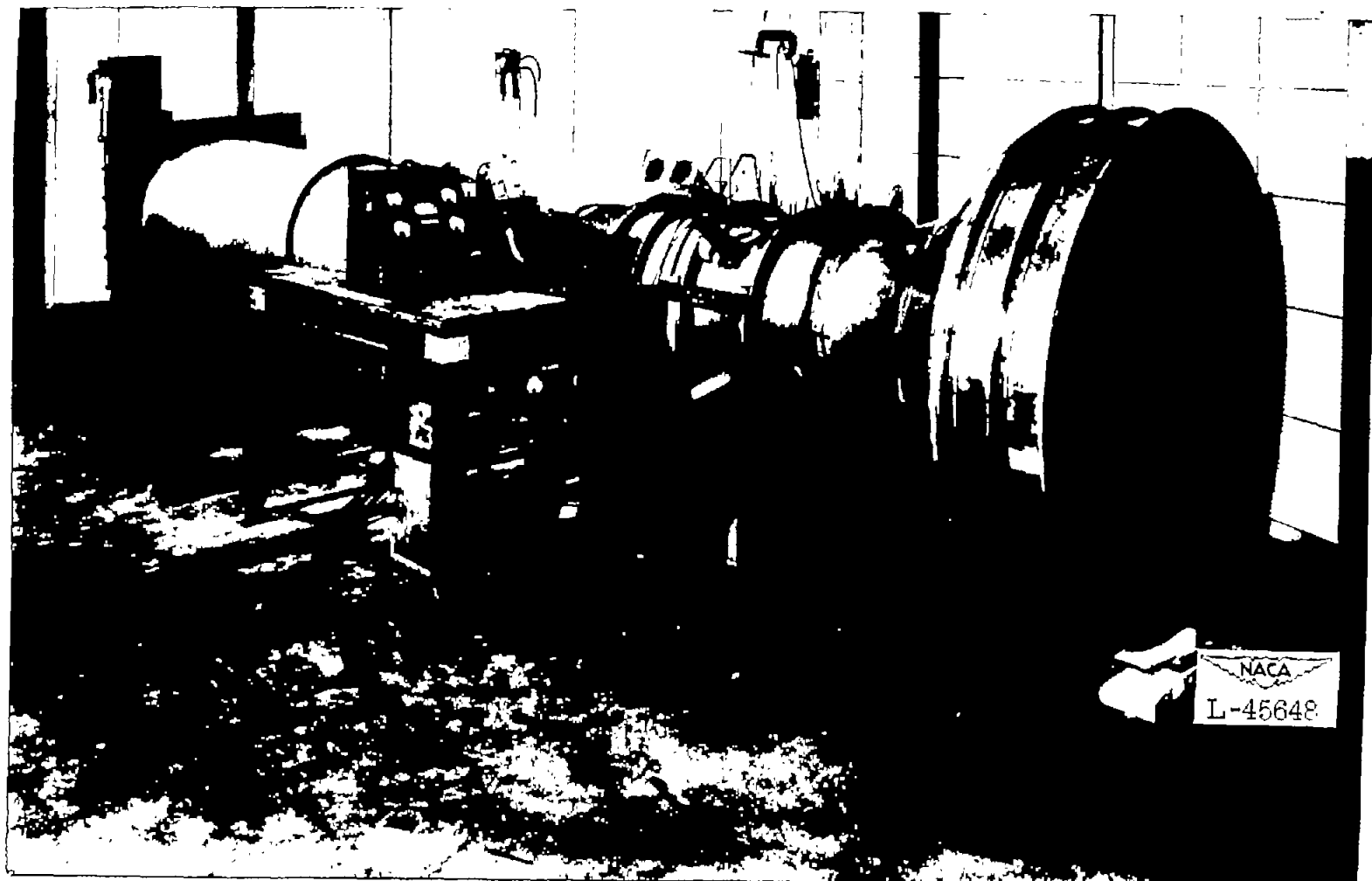
Figure 2.- Increase of total-pressure rise obtainable with rotors having solid-body and uniform tangential-velocity distributions as compared with total-pressure rise obtainable with free-vortex loaded rotor. The same tangential-velocity parameter at the hub is assumed for all three rotors.



(a) Constant axial velocity. (b) Varying axial velocity.

Figure 3.- Typical rotor velocity diagrams.



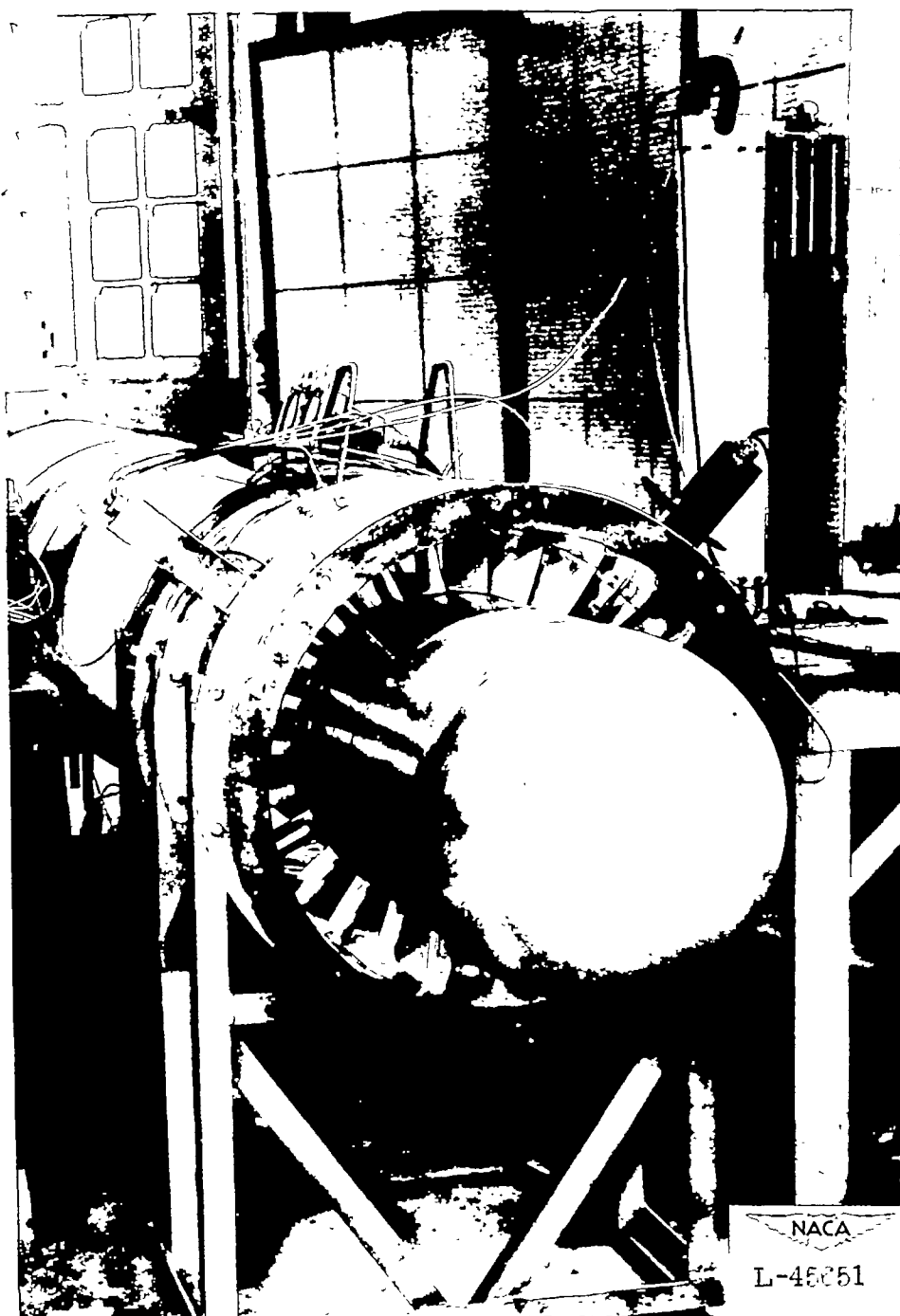


(a) Complete test setup.

Figure 4.- Views of test arrangement from entrance end.







(b) Entrance removed.

Figure 4.- Concluded.



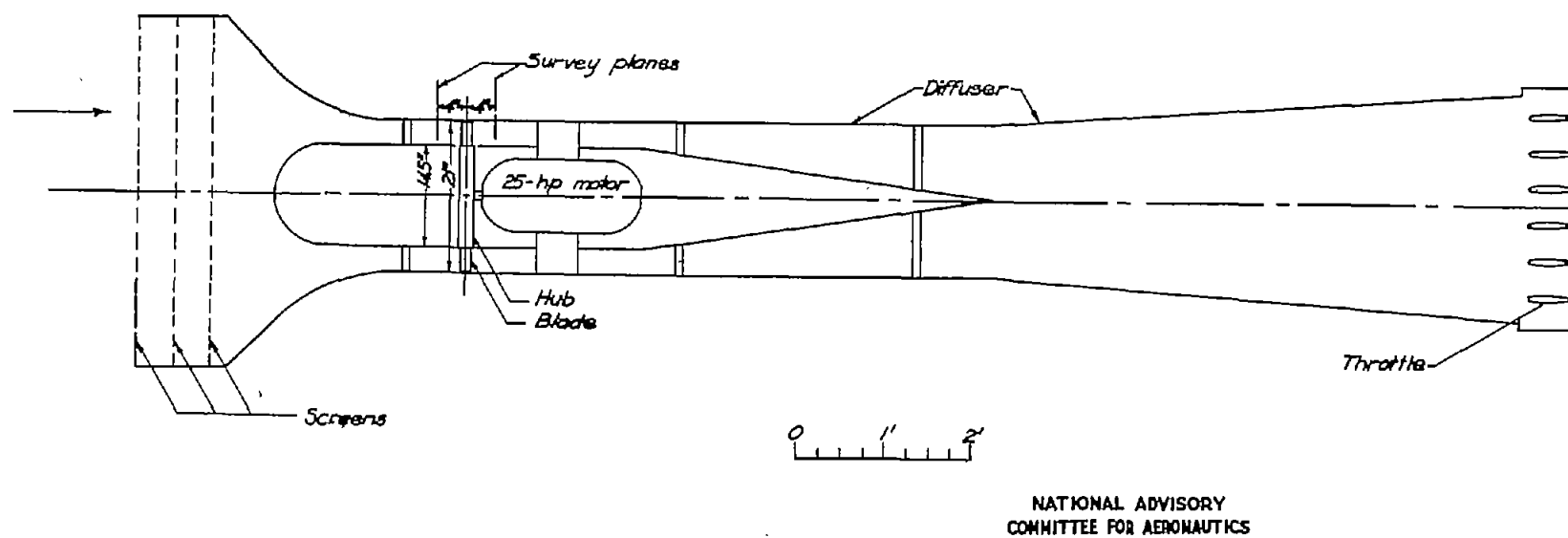
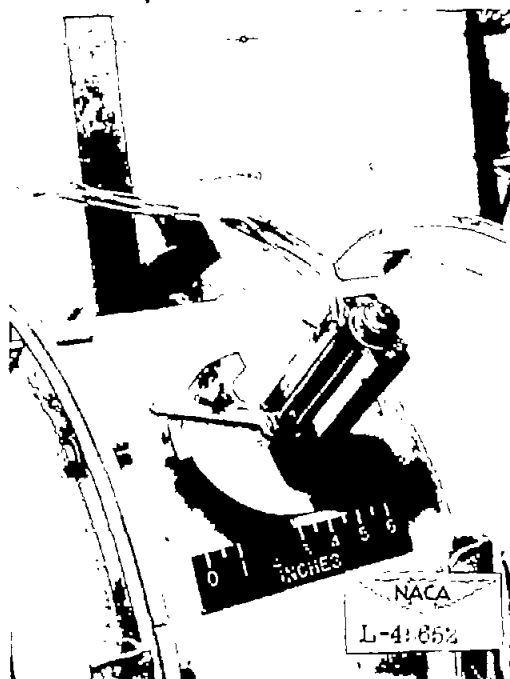
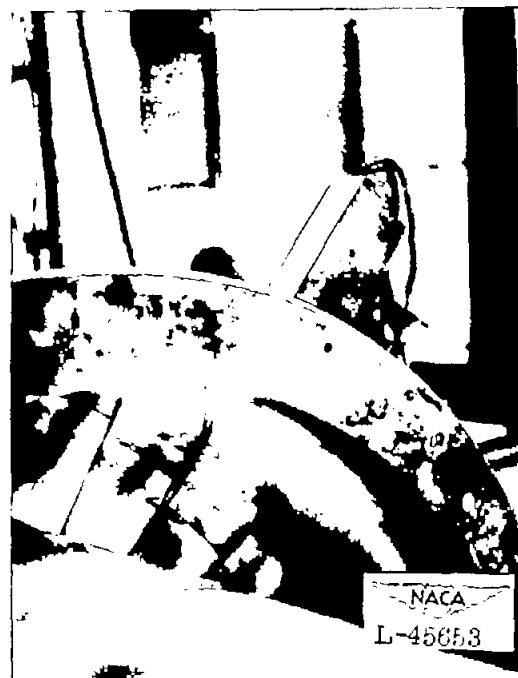


Figure 5.- Schematic drawing of test arrangement.

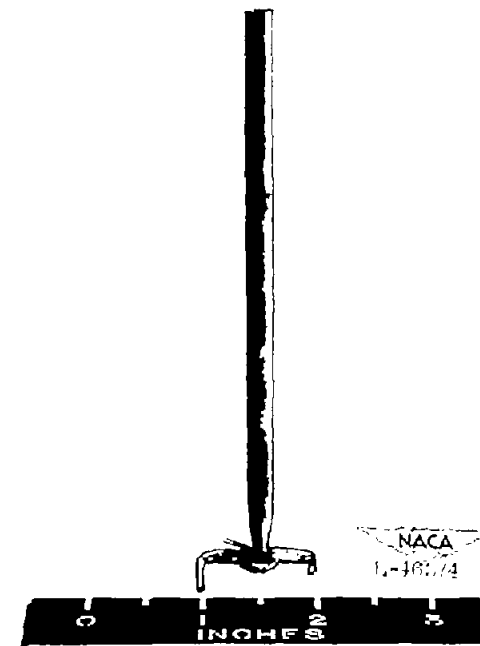




(a) External view.



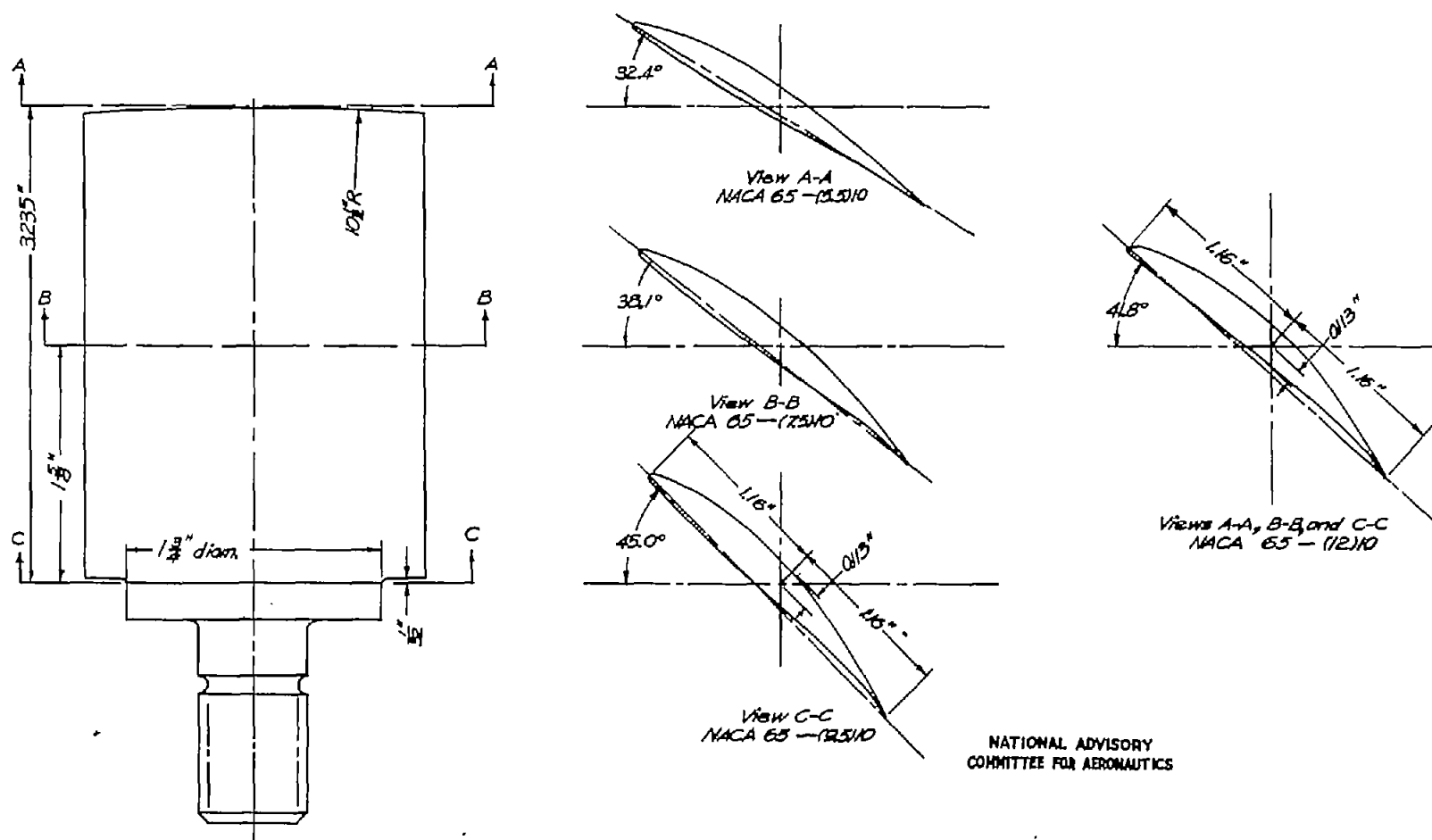
(b) Survey tube in duct.



(c) Detail view of survey tube.

Figure 6.- Views of survey instruments.





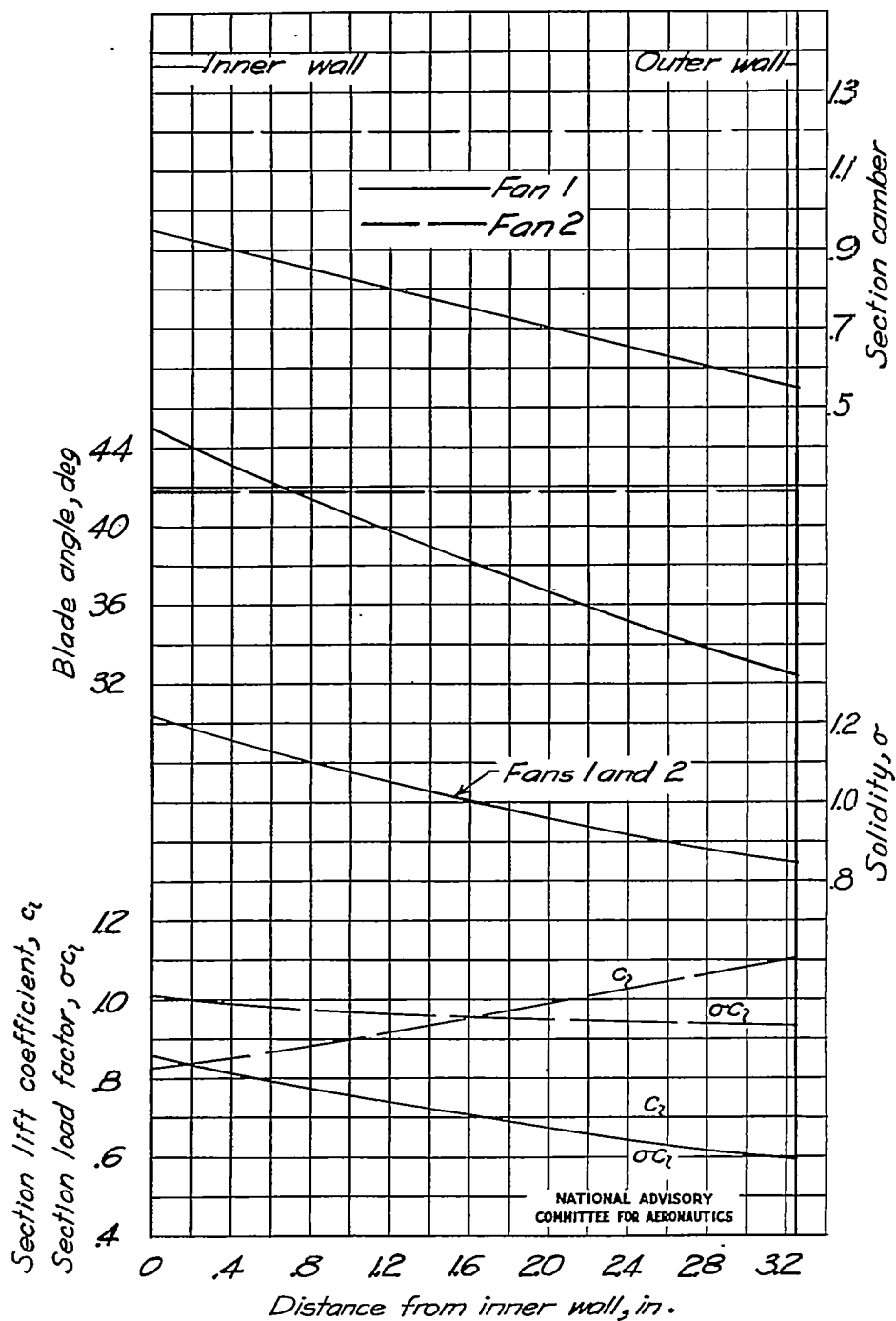
(a) Plan form.

(b) Fan 1 blade sections.

(c) Fan 2 blade section.

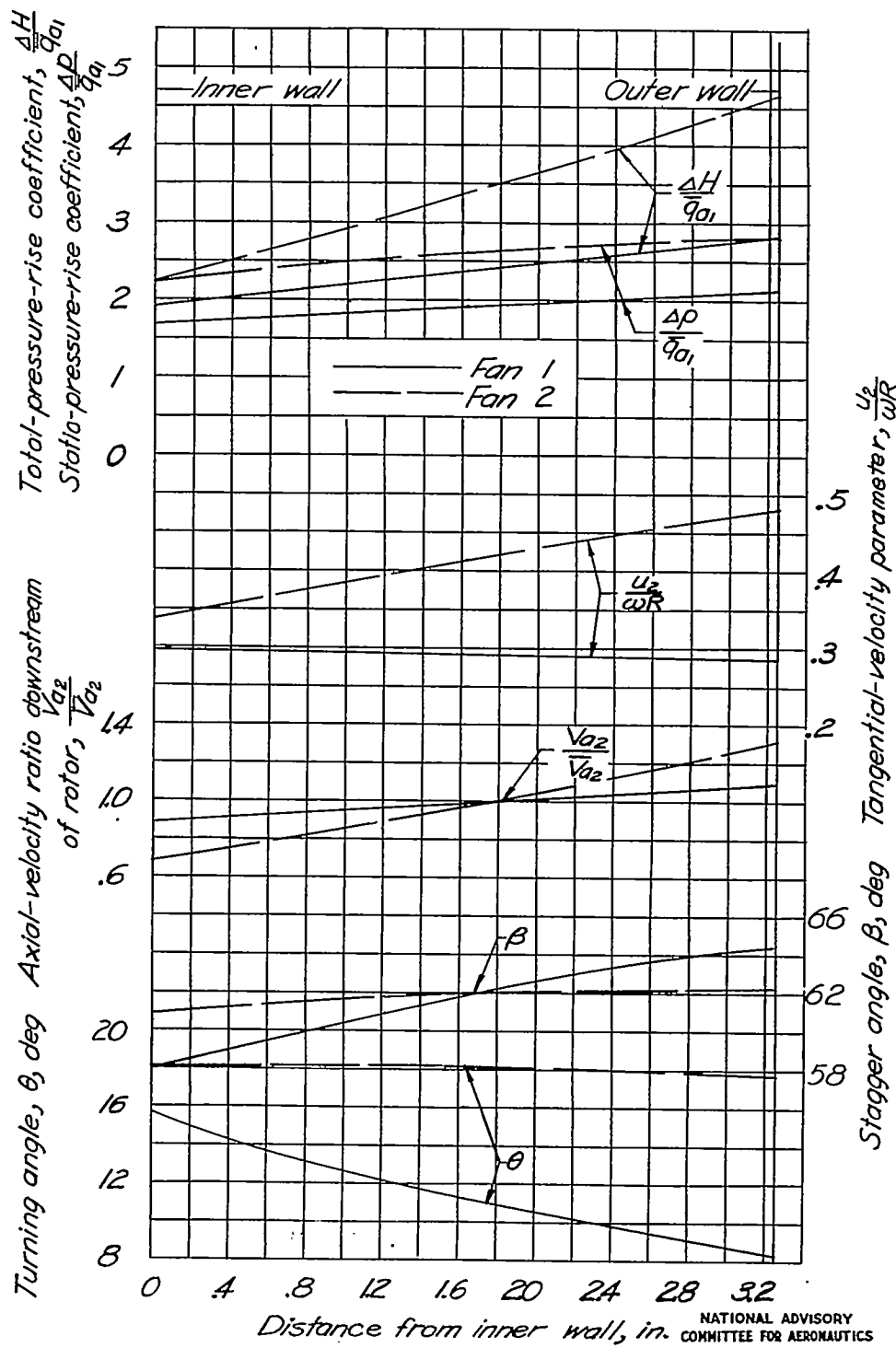
Figure 7.- Drawing of rotor blades.





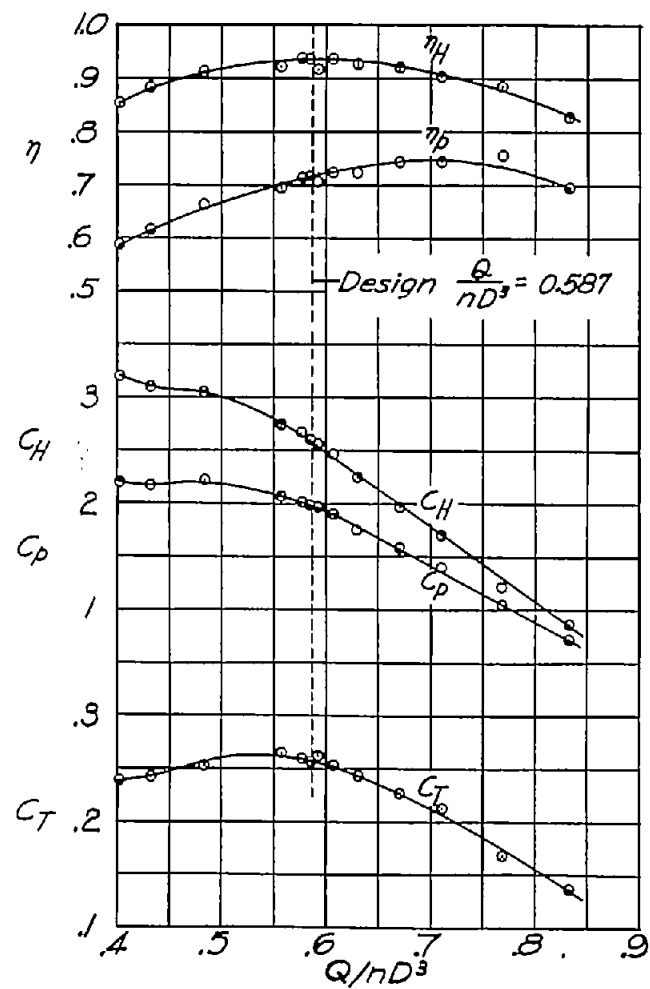
(a) Blade characteristics.

Figure 8.- Blade and theoretical performance characteristics of test rotors.

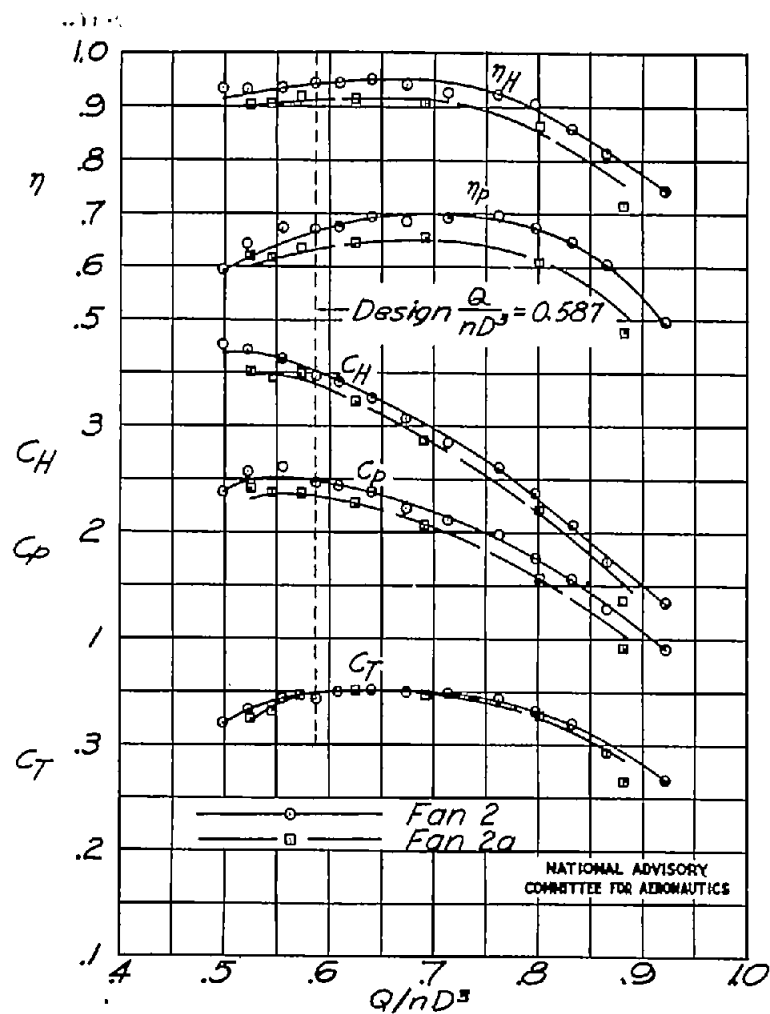


(b) Theoretical performance characteristics.

Figure 8.- Concluded.

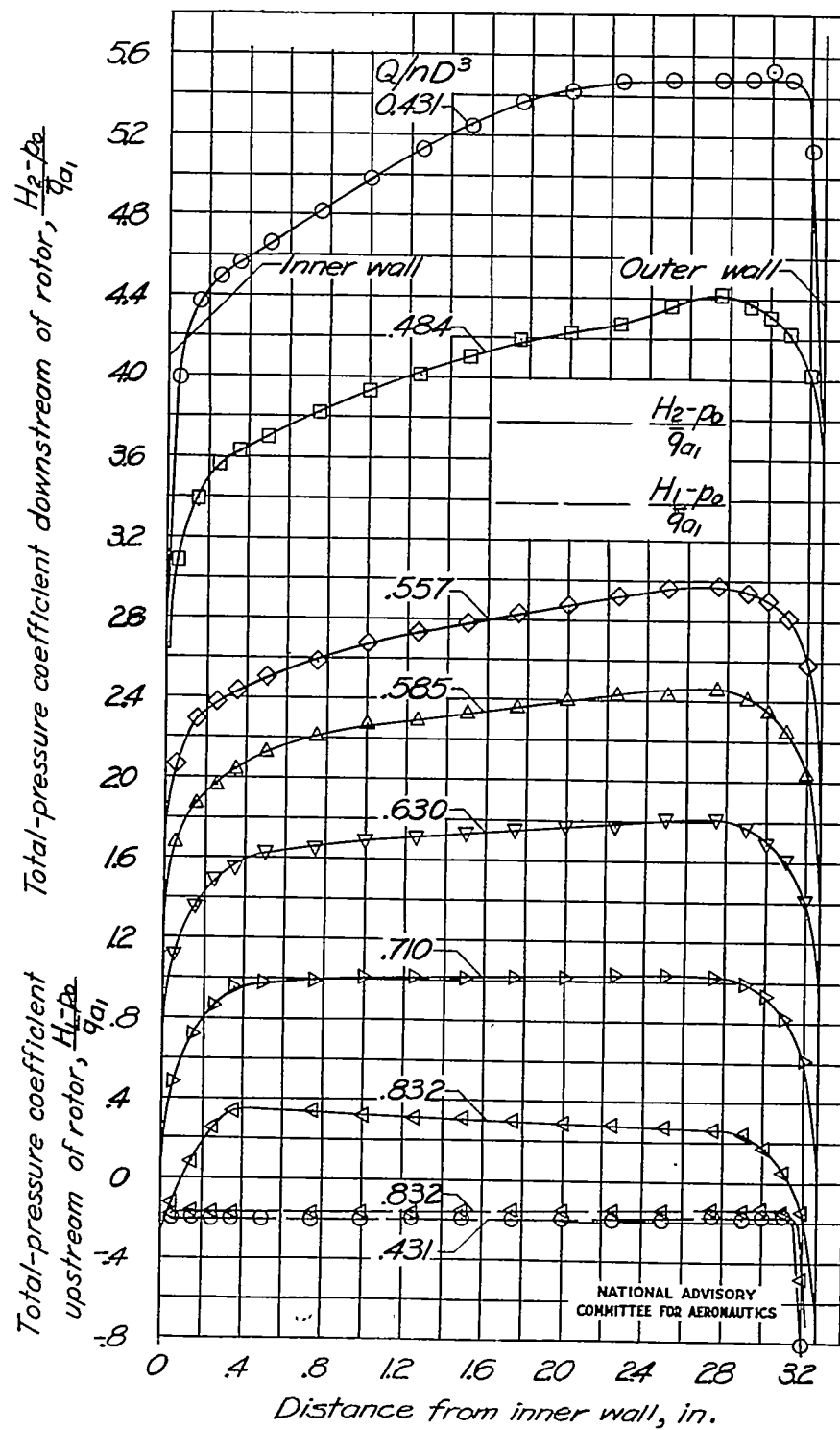


(a) Fan 1.



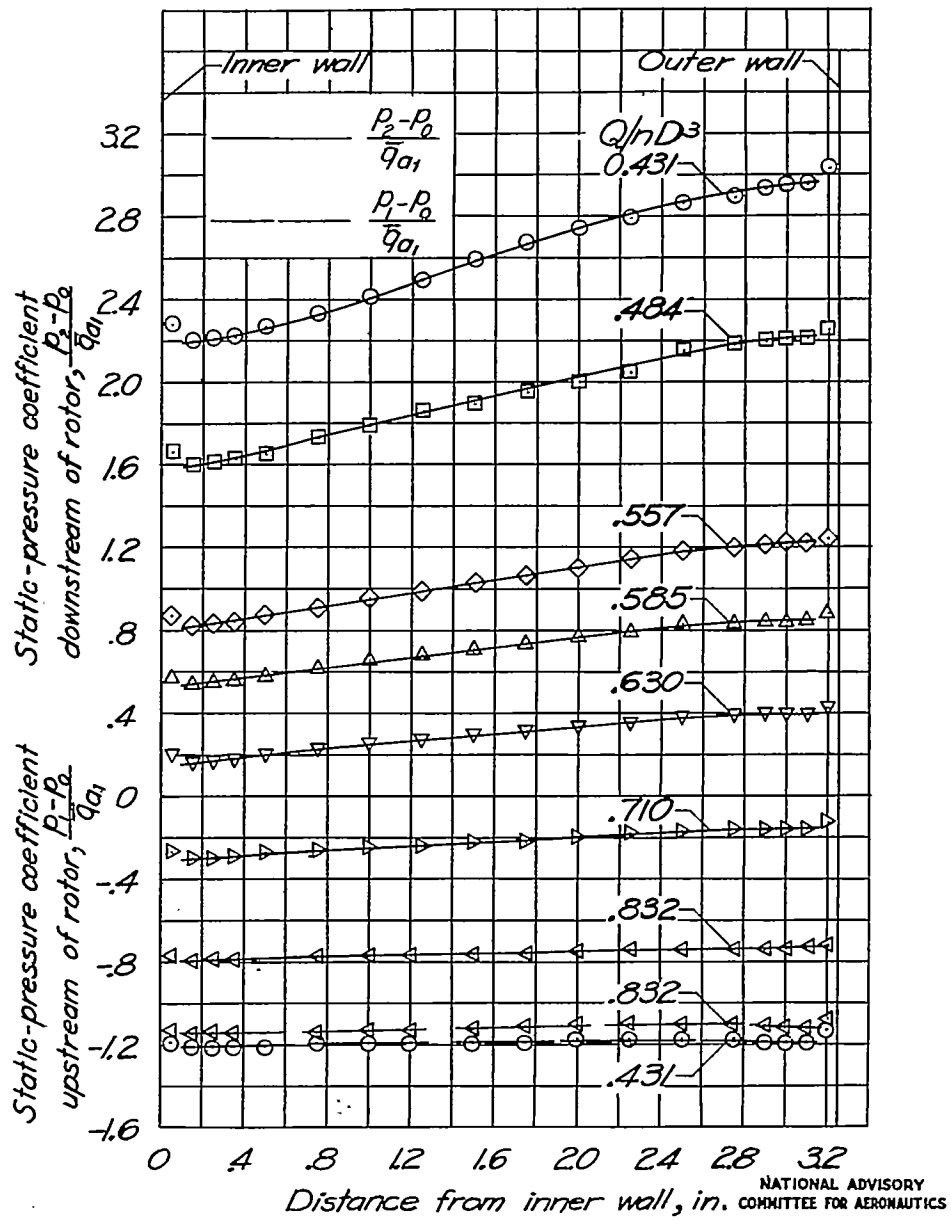
(b) Fans 2 and 2a.

Figure 9.- Over-all characteristic curves of fans 1, 2, and 2a.



(a) Total-pressure coefficient.

Figure 10.- Fan 1 survey results. Design  $\frac{Q}{nD^3} = 0.587$ .



(b) Static-pressure coefficient.

Figure 10.- Continued. Fan 1.

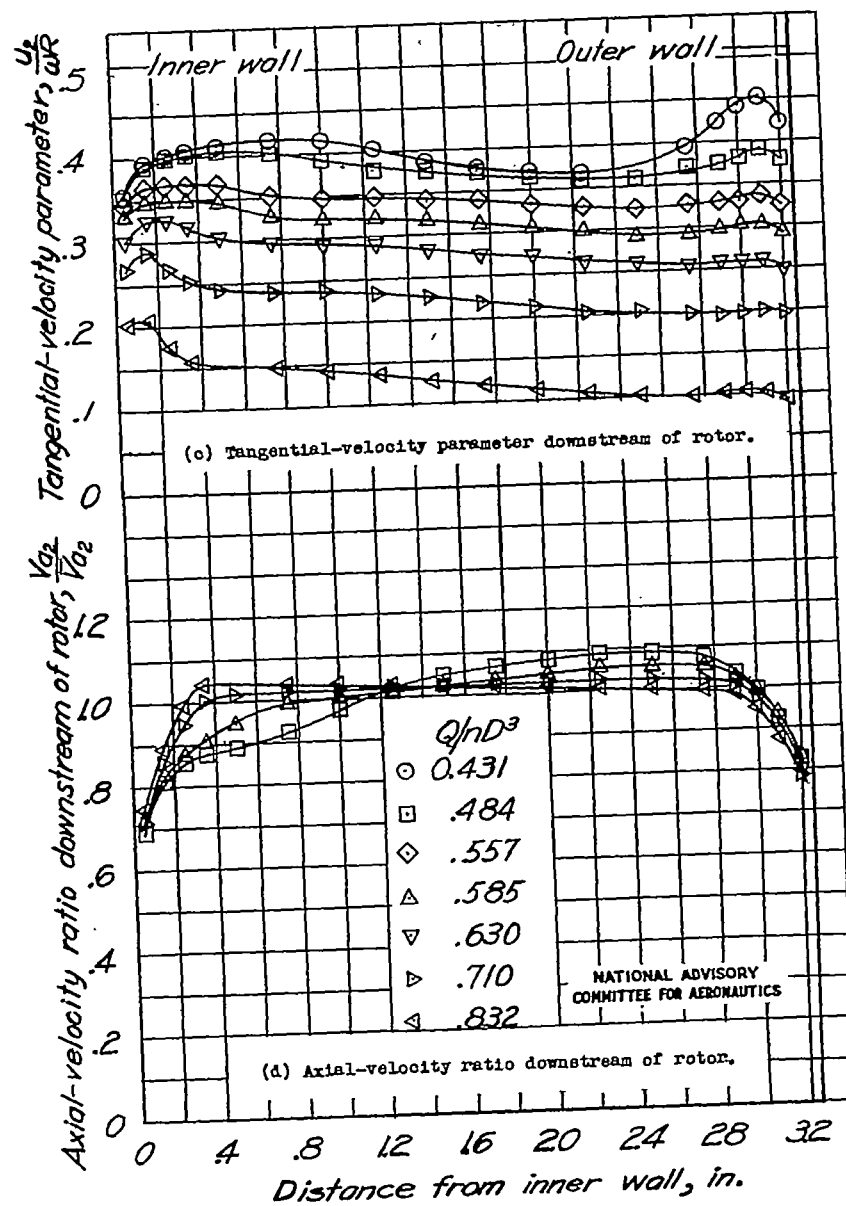


Figure 10.- Continued. Fan 1.

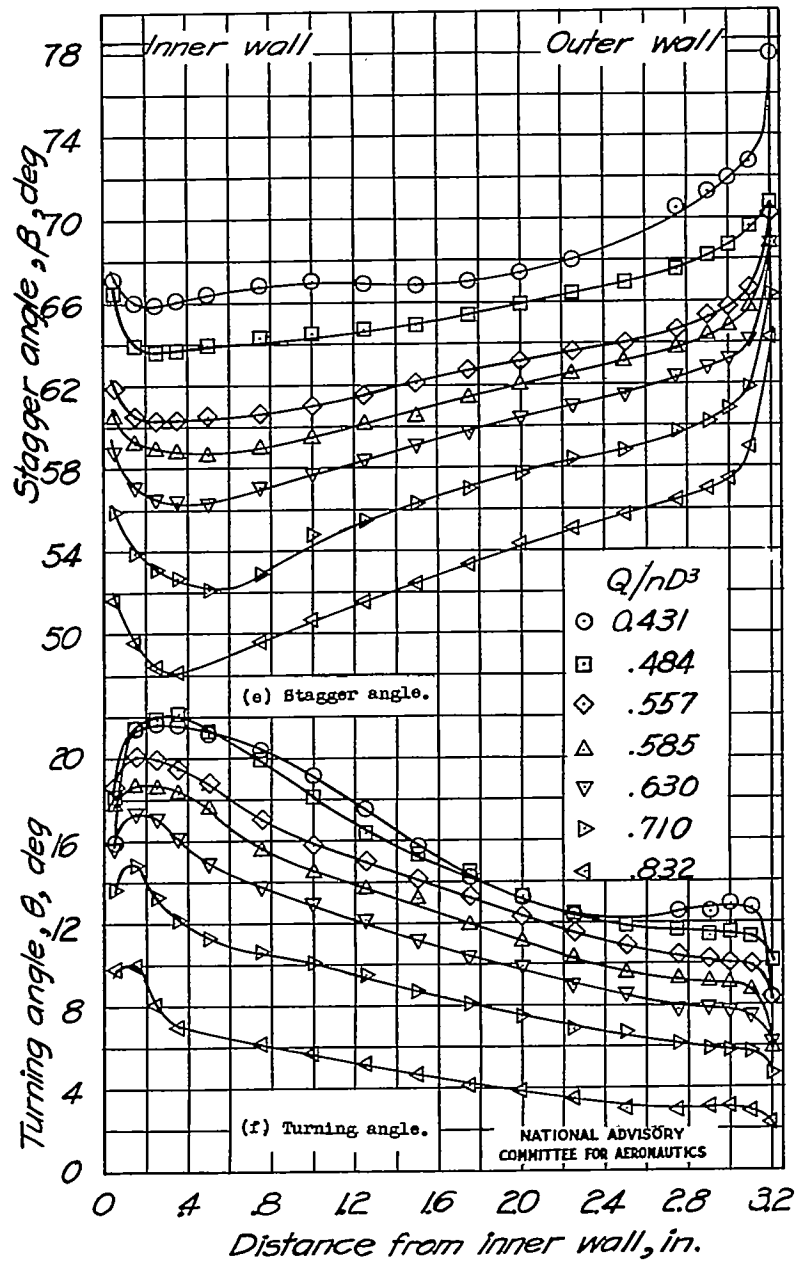
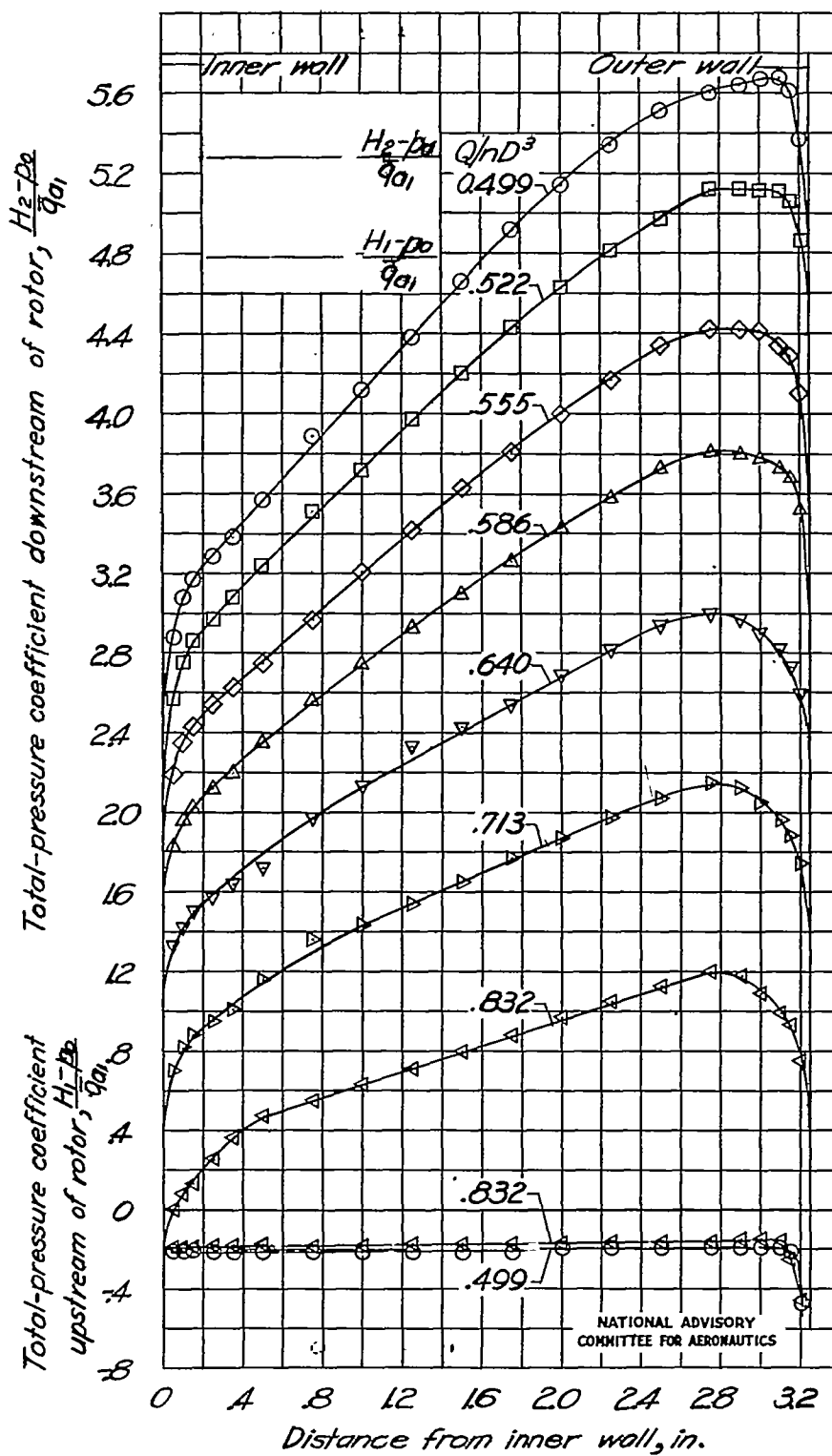


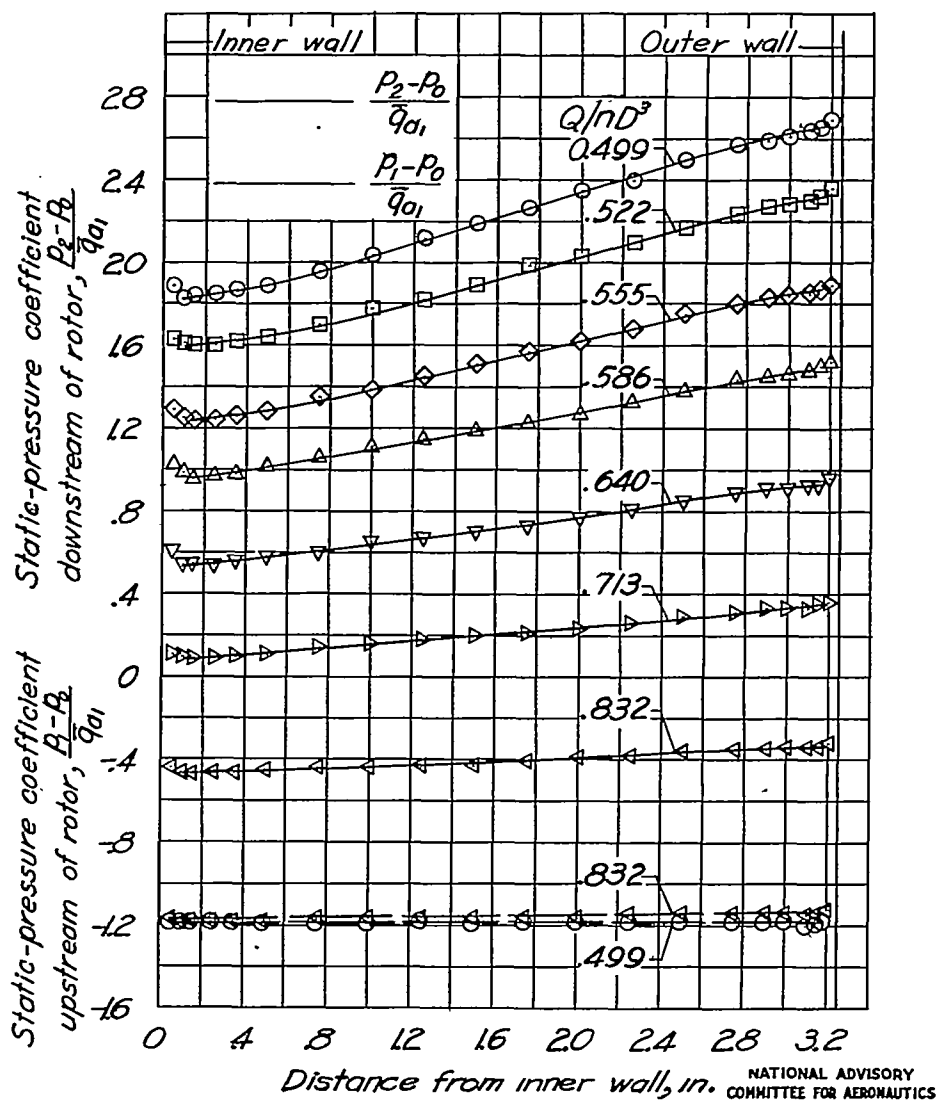
Figure 10.- Concluded. Fan 1.



(a) Total-pressure coefficient.

Figure 11.- Fan 2 survey results. Design  $\frac{Q}{nD^3} = 0.587$ .





(b) Static-pressure coefficient.

Figure 11.- Continued. Fan 2.

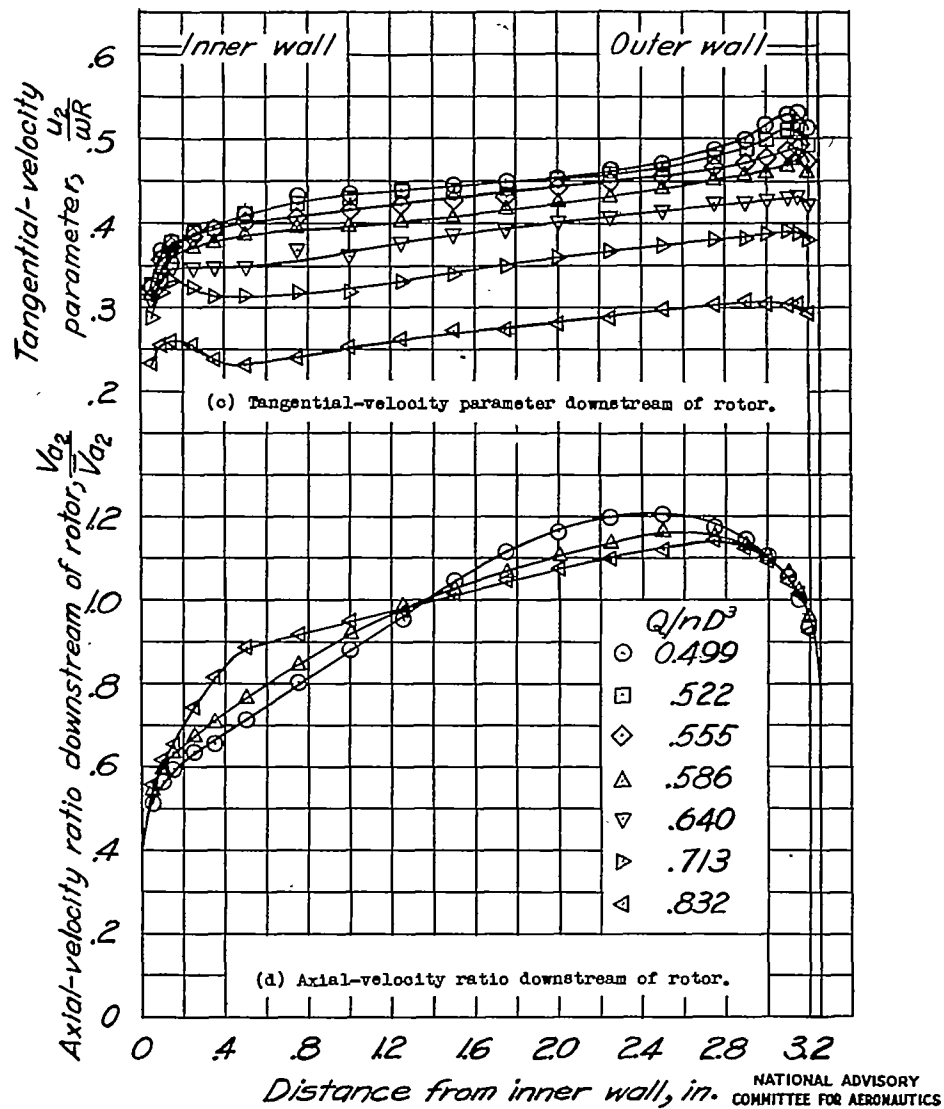


Figure 11.- Continued. Fan 2.

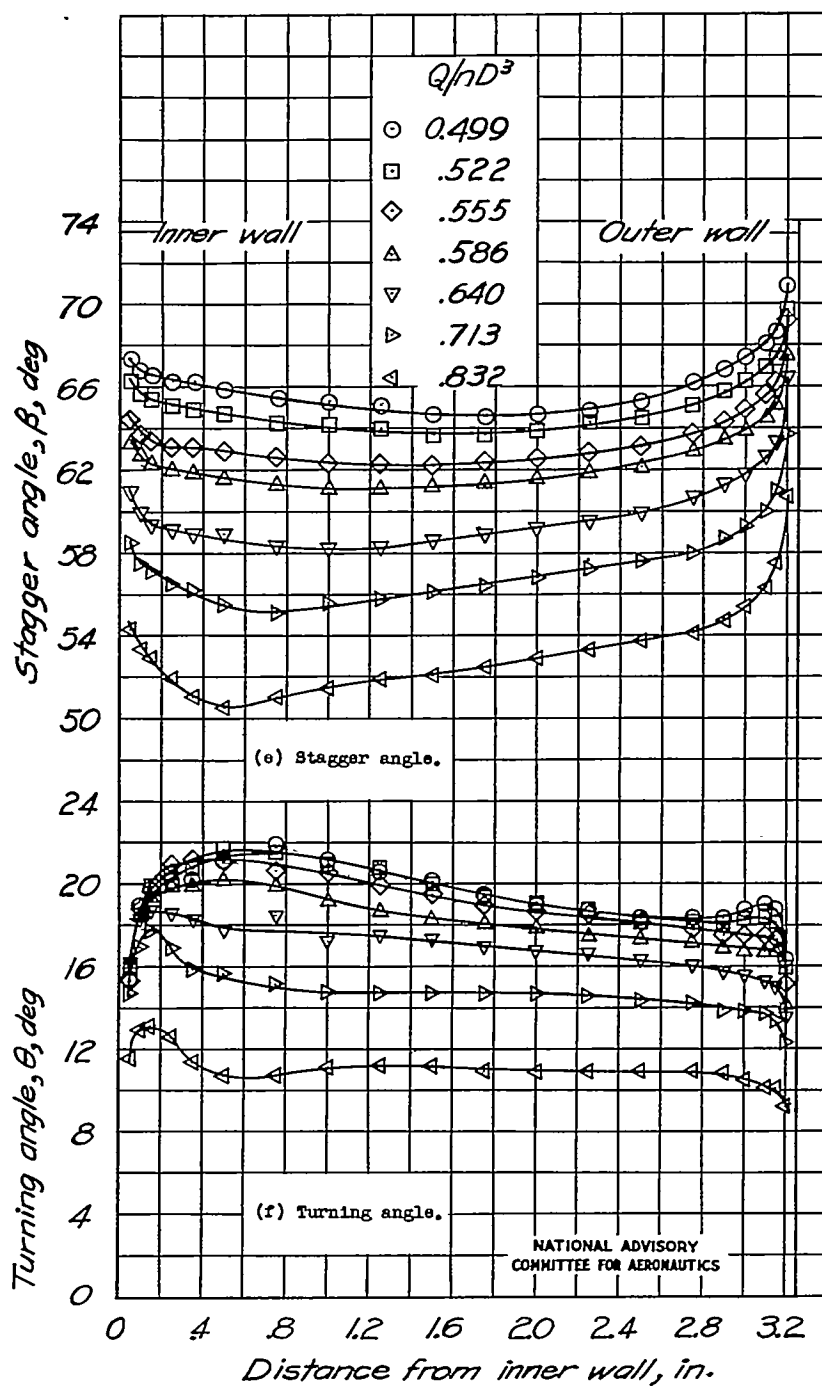
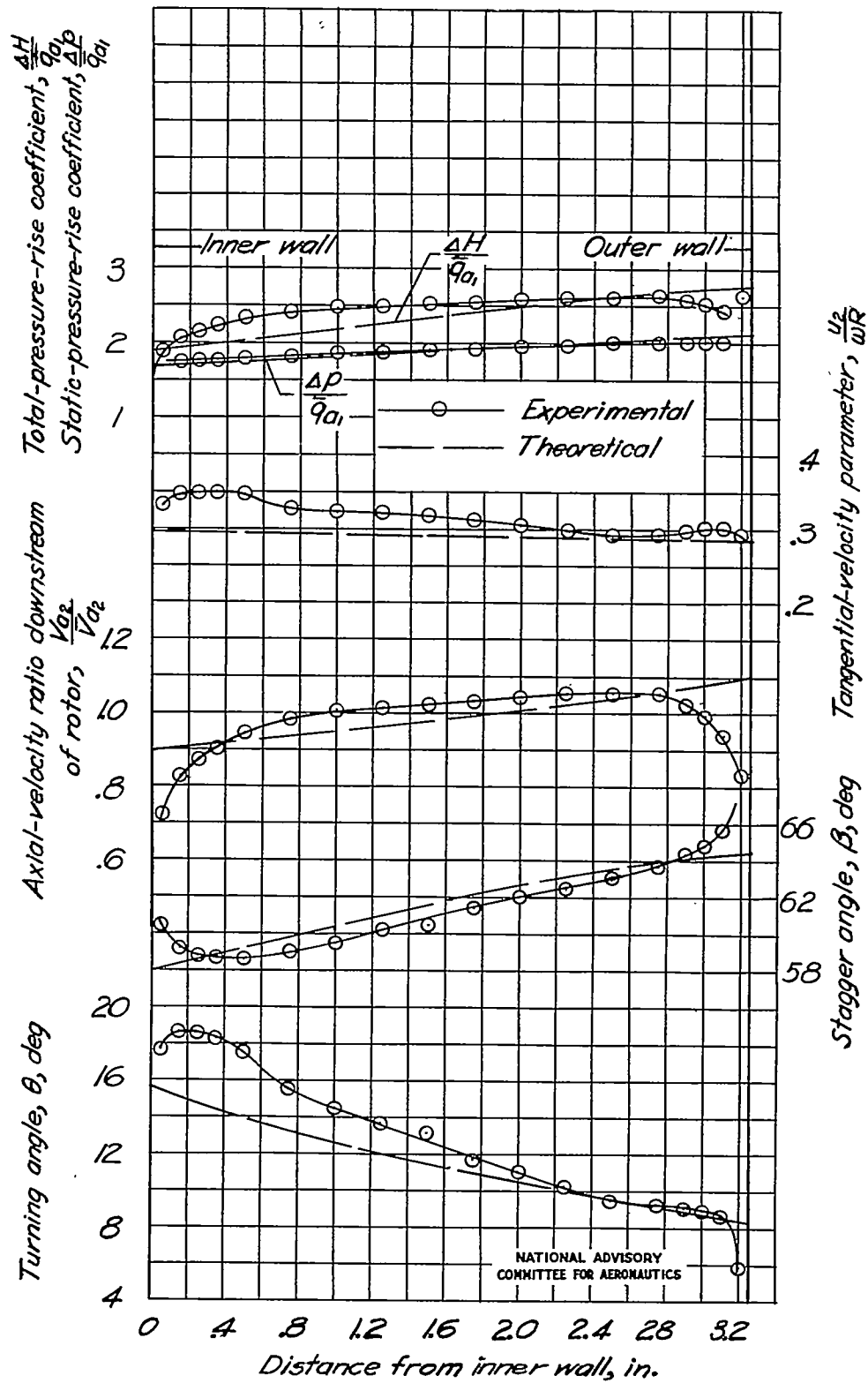
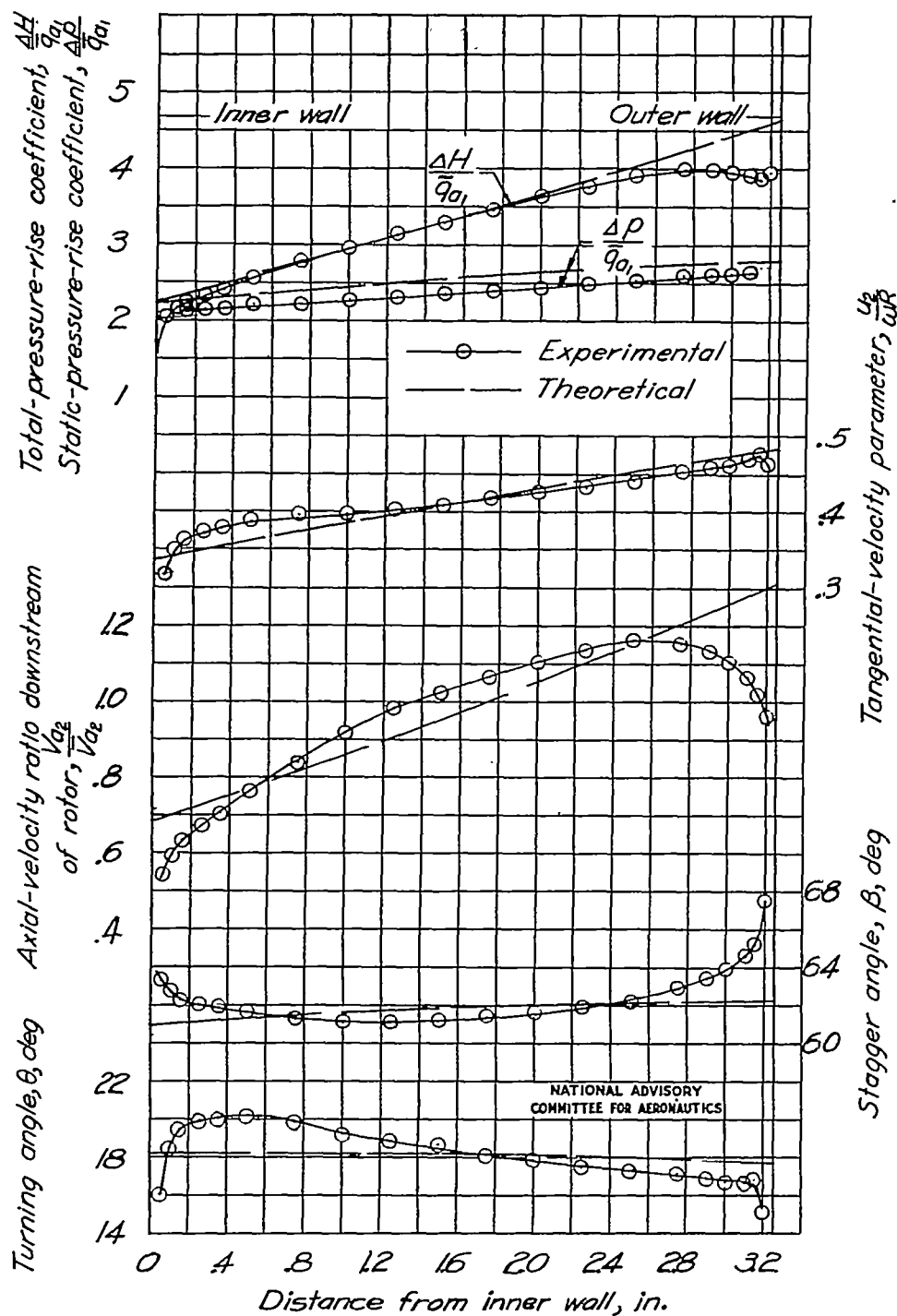


Figure 11.- Concluded. Fan 2.



(a) Fan 1.

Figure 12.- Comparison of experimental surveys with theory at design point.



(b) Fan 2.

Figure 12.- Concluded.

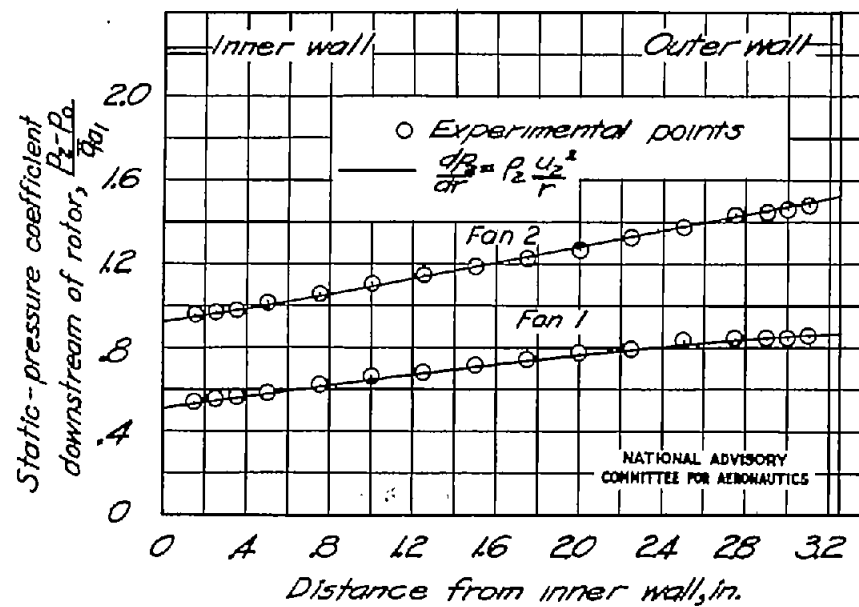
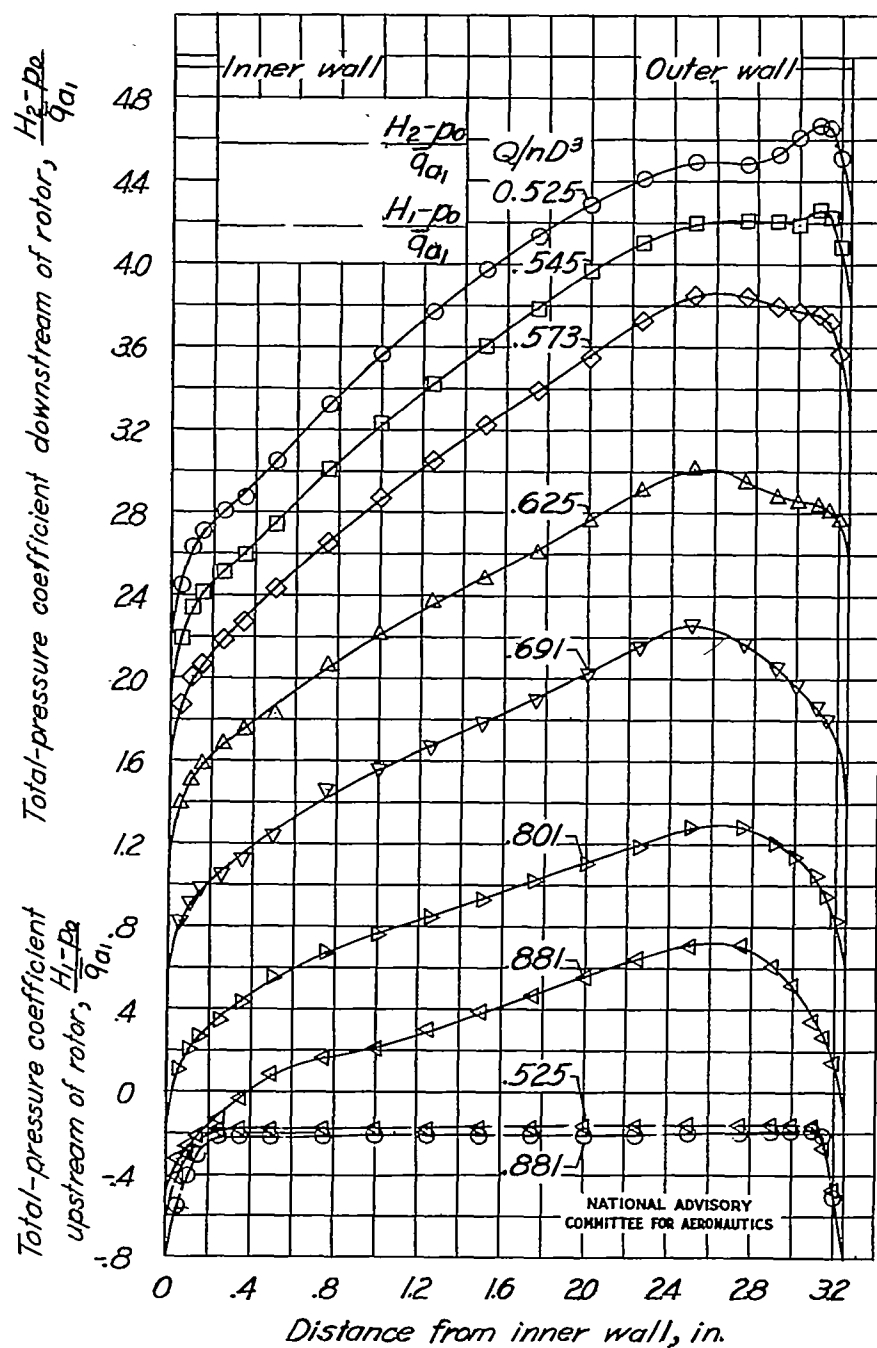
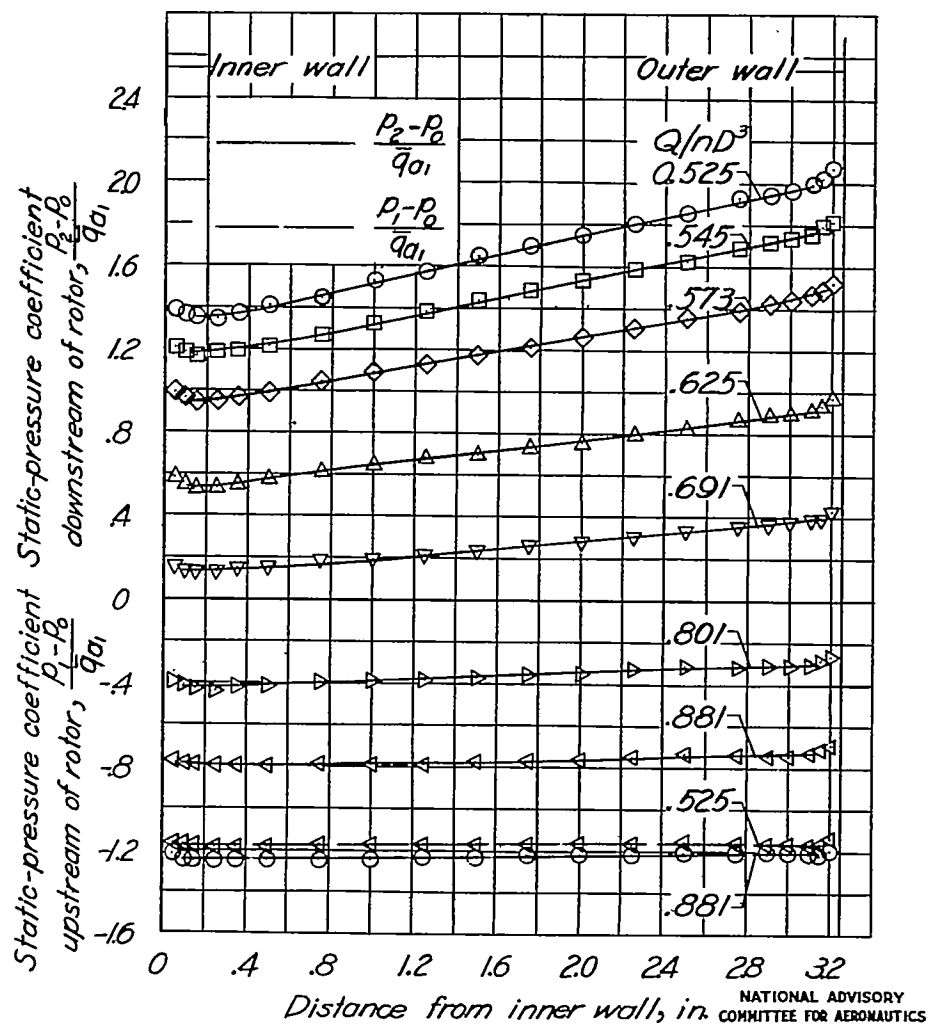


Figure 13.- Comparison of experimental and theoretical static-pressure gradients downstream of rotor.



(a) Total-pressure coefficient.

Figure 14.- Fan 2a survey results.



(b) Static-pressure coefficient.

Figure 14.- Continued. Fan 2a.



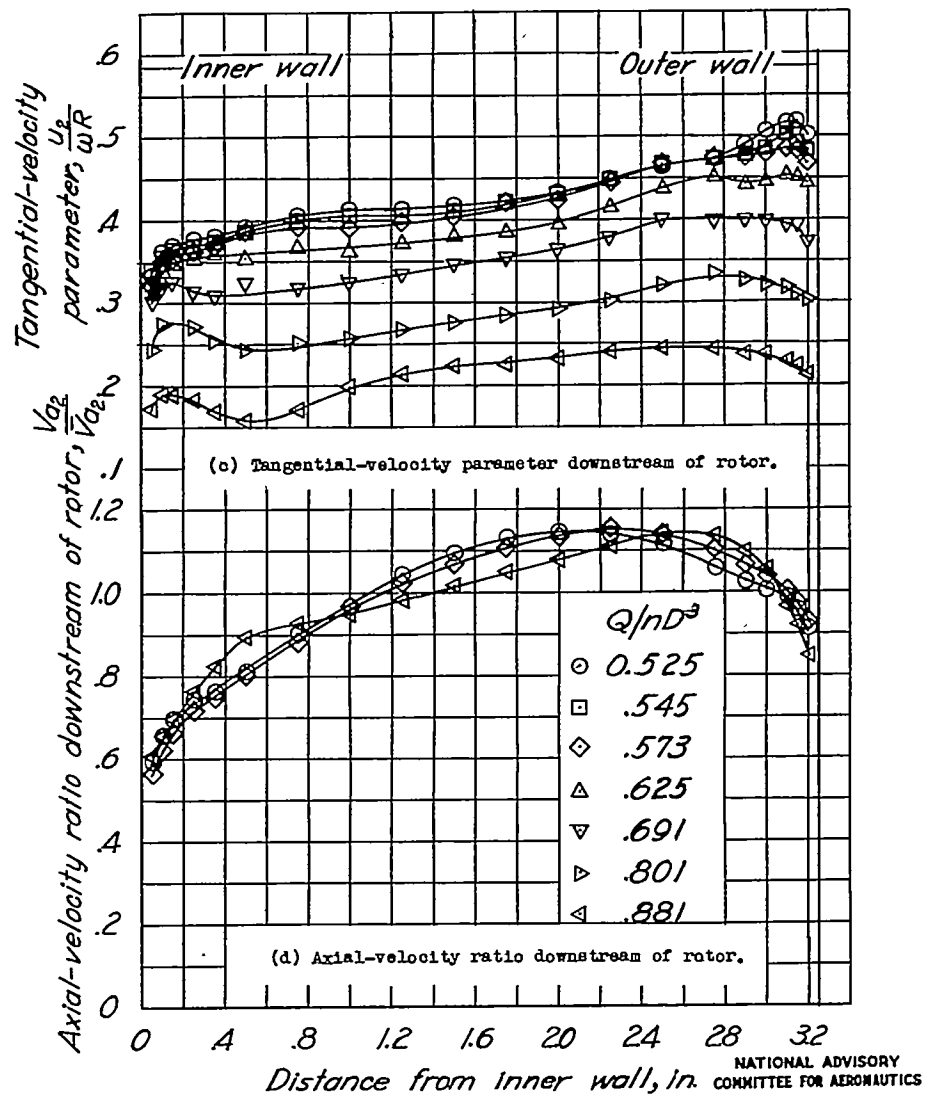


Figure 14.- Continued. Fan 2a.

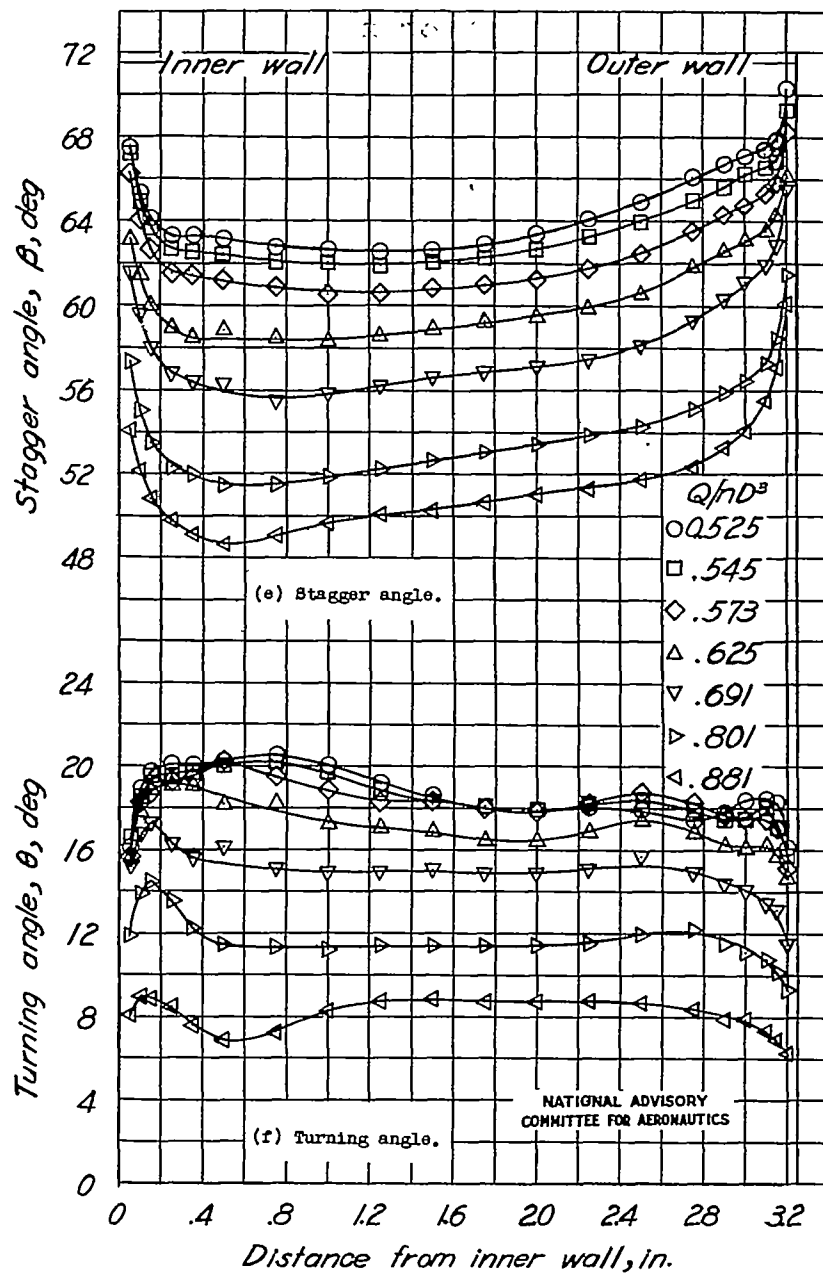


Figure 14.- Concluded. Fan 2a.

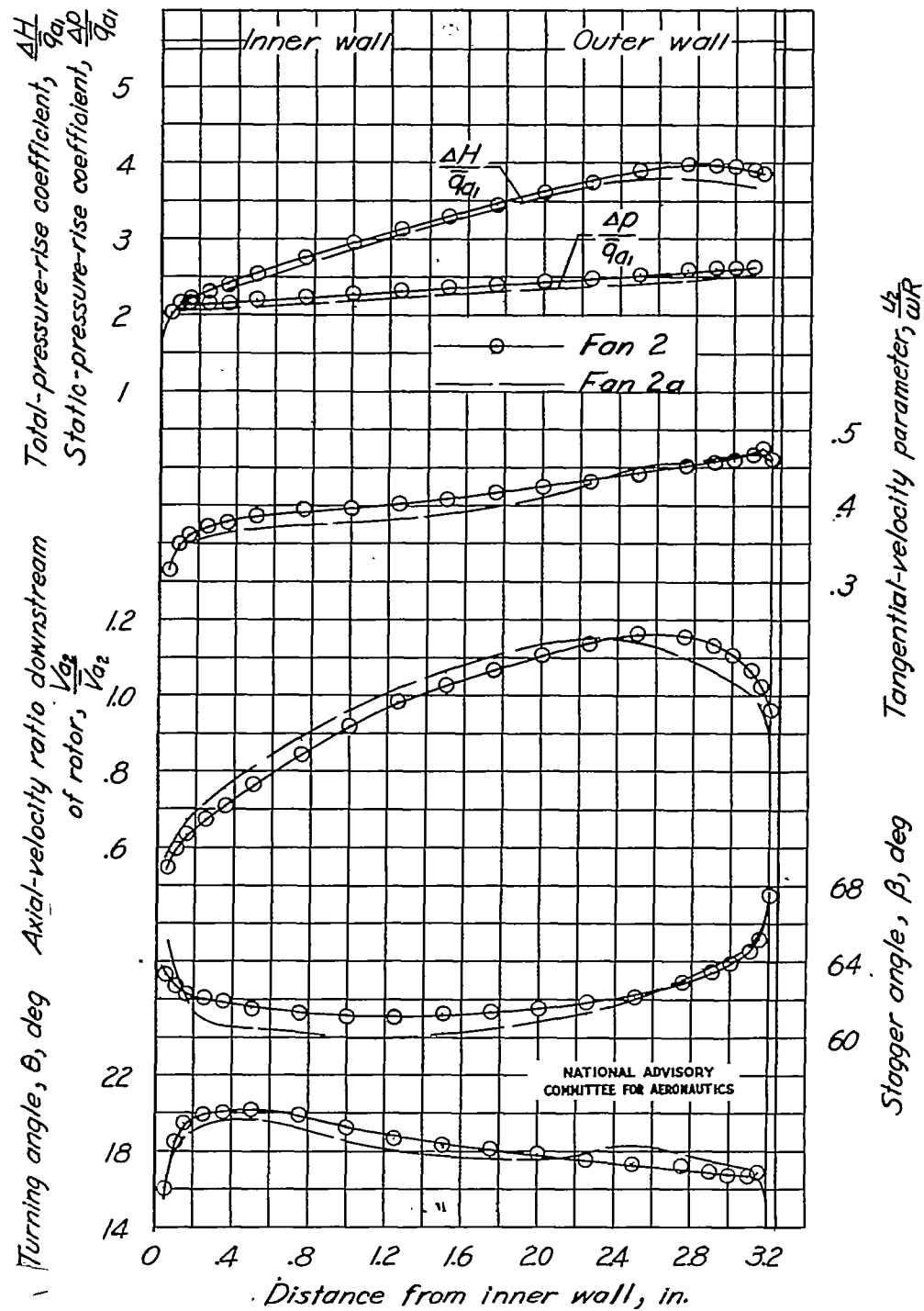


Figure 15.- Comparison of fan 2 and 2a survey results

$$\text{at } \frac{Q}{nD^3} = 0.586.$$